

# Systematic errors in the determination of Hubble constant due to the asphericity and non-isothermality of clusters of galaxies

Y.-G. Wang and Z.-H. Fan

*Department of Astronomy, Peking University, Beijing 100871, China*

wangyg@bac.pku.edu.cn, fan@bac.pku.edu.cn

## ABSTRACT

Joint analyses on X-ray and Sunyaev-Zel'dovich (SZ) effect of a cluster of galaxies can give rise to an estimate on the angular diameter distance to the cluster. With the redshift information of the cluster, the Hubble constant  $H_0$  can then be derived. Furthermore, such measurements on a sample of clusters with a range of redshift can potentially be used to discriminate different cosmological models. In this paper, we present statistical studies on the systematic errors in the determination of  $H_0$  due to the triaxiality and non-isothermality of clusters of galaxies. Different from many other studies that assume artificially a specific distribution for the intracluster gas, we start from the triaxial model of dark matter halos obtained from numerical simulations. The distribution of the intracluster gas is then derived under the assumption of the hydrodynamic equilibrium. For the equation of state of the intracluster gas, both the isothermal and the polytropic cases are investigated. We run Monte Carlo simulations to generate samples of clusters according to the distributions of their masses, axial ratios, concentration parameters, as well as line-of-sight directions. To mimic observations, the estimation of the Hubble constant is done by fitting X-ray and SZ profiles of a triaxial cluster with the isothermal and spherical  $\beta$ -model. We find that for a sample of clusters with  $M = 10^{14}h^{-1} M_\odot$  and  $z = 0.1$ , the value of the estimated  $H_0$  is positively biased with  $H_0^{peak}(estimated) \approx 1.05H_0(true)$  and  $H_0^{ave}(estimated) \approx 1.05H_0(true)$  for the isothermal case. For the polytropic case with  $\gamma = 1.15$ , the bias is rather large with  $H_0^{peak}(estimated) \approx 1.35H_0(true)$  and  $H_0^{ave}(estimated) \approx 3H_0(true)$ . For a mass-limited sample of clusters with  $M_{lim} = 10^{13}h^{-1} M_\odot$ , the results are similar. On the other hand, such a large overestimation has not been seen in real observations. It is noticed that the  $\beta$  value for observed clusters is within the range of 0.5 to 0.8. Considering only the subsample of clusters in Monte Carlo simulations with  $\beta$  in the range of 0.5 – 0.8, our analyses show that  $H_0^{ave}(estimated) = 1.002H_0(true)$  and

$H_0^{ave}(estimated) = 0.994H_0(true)$  for the isothermal and polytropic cases, respectively. We further find that the value of  $\beta$  is more sensitive to the intrinsic asphericity of clusters of galaxies than the axial ratio of two-dimensional X-ray images  $\eta$  is. Limiting to clusters with  $\beta \geq 0.5$  essentially excludes highly aspherical clusters from the sample. From this subsample of clusters, we can get a fair estimate on  $H_0$ .

*Subject headings:* distance scale— galaxies: cluster: general— dark matter

## 1. Introduction

The measurements of cosmological distances have played important roles in the development of cosmology. The discovery of the linear distance-redshift relation for galaxies in the 1920s (e.g., Hubble 1929) laid the observational foundation of the big bang cosmological theory. The accelerating expansion of the universe revealed by the observations on Type Ia supernovae points to the existence of dark energy, which has a profound impact on cosmology as well as on physics (e.g., Perlmutter et al. 1999; Riess et al. 1998). The commonly used distance measurements rely on various standard candles, such as Cepheid variables, Type Ia supernovae, and the Tully-Fisher relation. The calibration of one particular standard candle often involves another standard candle. This is the so called distance ladder. On the other hand, joint analyses of X-ray and the Sunyaev-Zel’dovich effect of a cluster of galaxies can give rise to an estimate of the angular diameter distance to the cluster. This method is independent of the distance ladder, and therefore provides an important test on the consistency of cosmological theories.

For clusters of galaxies, their typical mass is about  $10^{14} - 10^{15}M_\odot$ . Besides luminous galaxies, a large fraction of the baryonic matter in a cluster is in the form of hot intracluster gas. With a temperature of a few  $keV$ , the intracluster gas is fully ionized. Hot electrons emit strong X-ray through Bremsstrahlung processes (e.g., Rosati et al. 2002). Meanwhile, the electrons interact with Cosmic Microwave Background (CMB) photons and distort the CMB spectrum. The distortion due to the thermal motion of electrons is referred to as the thermal Sunyaev-Zel’dovich effect (SZ) (Sunyaev & Zel’dovich 1970, 1972). The Bremsstrahlung X-ray emission depends on the density of electrons through  $S_x \propto \int n_e^2 \Lambda_{eH}(T_e) dl$ , where  $n_e$  and  $T_e$  are the number density and temperature of electrons, respectively,  $\Lambda_{eH}$  is the X-ray cooling function, and the integration is along the line of sight. For the SZ effect, we have  $\delta T \propto \int n_e T_e dl$  (e.g., Carlstrom et al. 2002). From dimensional analyses, one can see that, up to a temperature-dependent factor, the quantity  $(\delta T)^2/S_x$  gives rise to an estimate of the dimension of the cluster along the line of sight. Under the assumption of spherical symmetry,

this size is the same as the linear extension of the cluster over the sky. With its measured angular size, one can then obtain the angular diameter distance to the cluster, and further the Hubble constant  $H_0$  (McHardy et al. 1990; Birkinshaw et al. 1991; Jones et al. 1993; Birkinshaw & Hughes 1994; Reese et al. 2002; Reese 2004; Schmidt et al. 2004).

Observationally, the spherical and isothermal  $\beta$  model is commonly used to describe the distribution of the intracluster gas. The two parameters in the model, the power index  $\beta$  and the characteristic scale  $r_c$ , are usually obtained by fitting the observed X-ray surface brightness with the  $\beta$  model. Thus any deviation from the sphericity and isothermality for the intracluster gas can introduce significant biases and uncertainties to the estimation of  $H_0$ . Studies have been performed on the effects of non-isothermality of the temperature profile, and the clumpiness and asphericity of the intracluster gas distribution (Birkinshaw et al. 1991; Inagaki et al. 1995; Roettiger et al. 1997; Cooray 1998; Hughes & Birkinshaw 1998; Sulkanen 1999; Puy et al. 2000; Udomprasert et al. 2004). It is noted that the non-isothermality can lead to about 20 – 30% errors in the  $H_0$  determination. The clumpiness and asphericity may introduce about 15% errors (e.g., Inagaki et al. 1995). Most of these studies either assume an aspherical gas distribution of a specific form, e.g., the triaxial  $\beta$  model (e.g., Sulkanen 1999), or concentrate on individual clusters from numerical simulations (e.g., Inagaki et al. 1995; Roettiger et al. 1997; Ameglio et al. 2005; Hallman et al. 2005). In this paper, rather than assuming an ad hoc gas distribution, we investigate the systematic errors starting from the triaxial mass distribution of dark matter halos. Our focus is on the statistical analyses for a sample of clusters generated from Monte Carlo simulations.

From numerical simulations, Jing and Suto (2002) proposed a triaxial model with specified statistics of the axial ratios for dark matter halos. The model has been applied to lensing studies (e.g., Oguri et al. 2003, 2004; Keeton et al. 2004; Tang & Fan 2005), to the distribution of intracluster gas (e.g., Lee & Suto 2003), and to the gas-associated X-ray and SZ effect of clusters of galaxies (Lee & Suto 2004; Wang & Fan 2004). In our current analyses on the systematic errors on  $H_0$  determination, we adopt the triaxial model for dark matter halos. The distribution of the intracluster gas and further the profiles of the X-ray surface brightness and SZ effect are derived under the assumption of hydrodynamic equilibrium. We consider both isothermal and polytropic equations of state for the intracluster gas. Regarding such distributions as ‘true’ distributions, the X-ray and SZ effect profiles are fitted with the spherical and isothermal  $\beta$  model. The two parameters  $\beta$  and  $r_c$  are obtained from the X-ray fitting alone as many observational analyses do. Then the estimated  $H_0$  and the true  $H_0$  are compared. The effects of the non-isothermality and the asphericity, as well as the effects of some other factors, are analyzed. To evaluate the biases and uncertainties statistically, we generate samples of clusters with Monte Carlo simulations. We take into account the distributions of the axial ratios and the concentration parameters of dark matter

halos. The mass function of dark matter halos is taken from Jenkins et al. (2001). Because of the asphericity of clusters, we also need to consider the statistics of line-of-sight directions in producing X-ray and SZ effect maps.

The rest of the paper is organized as follows. In §2, we present the intracluster gas distribution from the triaxial model of dark matter halos. In §3, we describe the  $H_0$  determination from the joint X-ray and SZ analysis. Our results are shown in §4 and §5. §6 contains conclusions and discussions.

## 2. Density distributions and temperature profiles of the intracluster gas

The dark matter distribution of clusters of galaxies is described by (Jing & Suto 2002)

$$\frac{\rho(R)}{\rho_{\text{crit}}} = \frac{\delta_c}{(R/R_0)^\alpha (1 + R/R_0)^{3-\alpha}} \quad (1)$$

where  $R = a(x^2/a^2 + y^2/b^2 + z^2/c^2)^{1/2}$  ( $c \leq b \leq a$ ) is the length of the major axis of a density contour,  $R_0$  is a characteristic scale,  $\delta_c$  is a dimensionless characteristic density contrast and  $\rho_{\text{crit}}$  is the critical density of the universe. We take  $\alpha = 1$  for clusters of galaxies.

We assume that the intracluster gas is in hydrodynamic equilibrium with the gravitational potential. Then the gas distribution is determined by

$$\frac{1}{\rho_g} \nabla P_g = - \nabla \Phi, \quad (2)$$

where  $P_g$  and  $\rho_g$  are the pressure and mass density of the intracluster gas, respectively, and  $\Phi$  is the gravitational potential from the total mass distribution. The specific gas distribution depends on its equation of state. For the isothermal gas, we have

$$\frac{\rho_g}{\rho_{g0}} = \exp \left[ -\frac{1}{K} (\Phi - \Phi_0) \right], \quad (3)$$

where  $K = k_B T_g / \mu m_p$ , in which  $k_B$ ,  $T_g$ ,  $\mu$ , and  $m_p$  represent the Boltzmann constant, the gas temperature, the mean molecular weight, and the proton mass, respectively. The subscript 0 denotes the corresponding value at the central position. For the polytropic gas satisfying the equation of state  $P_g \propto \rho_g^\gamma$ , its density and temperature distributions follow

$$\rho_g = \rho_{g0} \left[ 1 - \frac{1}{K_0} \frac{\gamma - 1}{\gamma} (\Phi - \Phi_0) \right]^{\frac{1}{\gamma-1}}, \quad (4)$$

$$T_g = T_{g0} \left[ 1 - \frac{1}{K_0} \frac{\gamma - 1}{\gamma} (\Phi - \Phi_0) \right], \quad (5)$$

where  $K_0 = k_B T_{g0} / \mu m_p$  with  $T_{g0}$  being the central temperature of the gas.

For a cluster of galaxies, the mass fraction of the gas is about 10%. Therefore its gravitational potential is dominantly determined by the dark matter component. Thus

$$\nabla^2 \Phi = 4\pi G \rho . \quad (6)$$

Given the triaxial mass distribution of the dark matter in eq.(1), the gravitational potential can be numerically calculated. Lee and Suto (2003) derived an analytical expression of  $\Phi$  under the approximation of small asphericity for dark matter halos. The perturbative solution can be written in the following form

$$\begin{aligned} \Phi(\mathbf{u}') = & C \left\{ F_1(u') + \frac{e_b^2 + e_c^2}{2} F_2(u') \right. \\ & + \frac{1}{2r'^2} \left[ e_b^2 (x' \cos \phi - y' \sin \phi \cos \theta + z' \sin \phi \sin \theta)^2 \right. \\ & \left. \left. + e_c^2 (y' \sin \theta + z' \cos \theta)^2 \right] F_3(u') \right\} \end{aligned} \quad (7)$$

where  $\mathbf{u}' = \mathbf{r}'/R_0$ ,  $\mathbf{r}' = (x', y', z')$  with  $z'$  being the line-of-sight direction,  $\theta$  and  $\phi$  are the polar coordinates of  $z'$  in the  $(x, y, z)$  coordinate system (Wang & Fan 2004),  $C = 4\pi G \delta_c \rho_{crit} R_0^2$ ,  $e_b = (1 - b^2/a^2)^{1/2}$  and  $e_c = (1 - c^2/a^2)^{1/2}$ . Here  $e_b$  and  $e_c$  are the two eccentricities of the ellipsoidal dark matter halos. The three functions  $F_1(u')$ ,  $F_2(u')$  and  $F_3(u')$  are given in Lee and Suto (2003). Wang and Fan (2004) further derived the X-ray and SZ profiles under the perturbative approximation, which are the main formulations to be used in our following analyses.

### 3. Estimates on the Hubble constant

In the observational analyses on X-ray and SZ effect of a cluster of galaxies, the spherical and isothermal  $\beta$  model is widely adopted to describe the distribution of the intracluster gas. With this model, the number density and the temperature of electrons are

$$n_e = n_{e0} [1 + (r/r_c)^2]^{-3\beta/2}, \quad (8)$$

$$T_e = T_{e0}, \quad (9)$$

where  $n_{e0}$  is the central number density of electrons,  $r_c$  is the core radius, and  $\beta$  represents the slope of the profile. The corresponding X-ray and SZ effect profiles are

$$S_x = S_{x0} [1 + (\theta/\theta_c)^2]^{1/2-3\beta}, \quad (10)$$

and

$$\delta T = \delta T_0 [1 + (\theta/\theta_c)^2]^{1/2-3\beta/2}. \quad (11)$$

where  $\theta = r/D_A$  with  $D_A$  being the angular diameter distance to the cluster. In the  $\beta$  model, the central values  $S_{x0}$  and  $\delta T_0$  depend on  $n_{e0}$ ,  $\theta_c$ ,  $\beta$  and  $D_A$ . Observationally,  $S_{x0}$  and  $\delta T_0$  are measurable quantities, and  $\theta_c$  and  $\beta$  are usually obtained through the fitting to the X-ray profile. Thus by eliminating  $n_{e0}$ , the angular diameter distance  $D_A$  can be estimated by (e.g., Reese et al. 2002)

$$D_A(\text{estimated}) = \frac{(\delta T_0)^2}{S_{x0}} \left( \frac{m_e c^2}{k_B T_{e0}} \right)^2 \frac{\Lambda_{eH0} \mu_e / \mu_H}{4\pi^{3/2} \mathfrak{R}_{(x,T_e)}^2 T_{CMB}^2 \sigma_T^2 (1+z)^4 \theta_c} \frac{1}{G(\beta)} \quad (12)$$

where  $G(\beta) = [\Gamma(3/2\beta - 1/2)/\Gamma(3/2\beta)]^2 \Gamma(3\beta)/\Gamma(3\beta - 1/2)$  with  $\Gamma(\beta)$  being the Gamma function, and  $\mathfrak{R}_{(x,T_e)}$  is the frequency-dependent factor for the SZ effect with  $x = h\nu/k_B T_{CMB}$ . The quantities  $h$ ,  $k_B$ ,  $c$ ,  $m_e$ ,  $\sigma_T$  and  $T_{CMB}$  are the Planck constant, the Boltzmann constant, the speed of light, the electron mass, the Thomson cross section, and the CMB temperature, respectively. The X-ray cooling function is denoted by  $\Lambda_{eH0}$  for  $T_e = T_{e0}$ , and  $n_H = n_e \mu_e / \mu_H$  with  $n_j = \rho_j / \mu_j m_p$  for species  $j$ . From the functional form of  $G(\beta)$ , it is noted that eq.(12) can be used only with  $\beta > 1/3$ .

For a cluster with its gas distribution being different from that of the spherical and isothermal  $\beta$  model, the estimated  $D_A$  deviates from the true  $D_A$ . Thus systematic errors are introduced in the  $H_0$  determination. In our analyses, we treat the gas distribution resulting from the triaxial model of dark matter halos as the 'true' gas distribution. For the isothermal case, the electron number density from the triaxial model can be approximated by (Wang & Fan 2004)

$$\begin{aligned} n_e = & n_{e0} \exp \left\{ -\frac{C}{K} \left\{ F_1(u') + \frac{e_b^2 + e_c^2}{2} F_2(u') \right. \right. \\ & + \frac{1}{2r'^2} \left[ e_b^2 (x' \cos \phi - y' \sin \phi \cos \theta + z' \sin \phi \sin \theta)^2 \right. \\ & \left. \left. + e_c^2 (y' \sin \theta + z' \cos \theta)^2 \right] F_3(u') \right\} \}. \end{aligned} \quad (13)$$

The corresponding SZ effect and the X-ray profiles are

$$\begin{aligned} \delta T &= \mathfrak{R}_{(x,T_e)} T_{CMB} D_A(\text{true}) \theta_0 \int \sigma_T \frac{k_B T_e}{m_e c^2} n_e d(z'/R_0) \\ &= n_{e0} \mathfrak{R}_{(x,T_e)} T_{CMB} D_A(\text{true}) \theta_0 \sigma_T \frac{K_B T_e}{m_e c^2} f(\theta_x/\theta_0, \theta_y/\theta_0, c_e, e_b, e_c, \theta, \phi), \end{aligned} \quad (14)$$

and

$$S_x = \frac{1}{4\pi(1+z)^4} D_A(\text{true}) \theta_0 \int \frac{\mu_e}{\mu_H} n_e^2 \Lambda_{eH} d(z'/R_0)$$

$$= n_{e0}^2 \frac{1}{4\pi(1+z)^4} D_A(true) \theta_0 \frac{\mu_e}{\mu_H} \Lambda_{eH} g(\theta_x/\theta_0, \theta_y/\theta_0, c_e, e_b, e_c, \theta, \phi), \quad (15)$$

where  $f = 1/n_{e0} \int n_e d(z'/R_0)$ ,  $g = 1/n_{e0}^2 \int n_e^2 d(z'/R_0)$ ,  $\theta_0 = R_0/D_A(true)$  is the angular scale radius, and  $z$  is the redshift of the cluster. Then we have

$$D_A(true) = \frac{(\delta T_0)^2}{S_{x0}} \left( \frac{m_e c^2}{k_B T_{e0}} \right)^2 \frac{\Lambda_{eH0} \mu_e / \mu_H}{4\pi \mathfrak{R}_{(x, T_e)}^2 T_{CMB}^2 \sigma_T^2 (1+z)^4} \frac{1}{\theta_0} \frac{g(0, 0, C/K, e_b, e_c, \theta, \phi)}{f^2(0, 0, C/K, e_b, e_c, \theta, \phi)}. \quad (16)$$

Comparing  $D_A(true)$  and  $D_A(estimated)$ , we obtain

$$\frac{D_A(true)}{D_A(estimated)} = \pi^{1/2} G(\beta) \frac{\theta_c}{\theta_0} \frac{g(0, 0, c_e, e_b, e_c, \theta, \phi)}{f^2(0, 0, c_e, e_b, e_c, \theta, \phi)}. \quad (17)$$

Given a cosmological model, we have  $D_A \propto H_0^{-1}$ , therefore,

$$\begin{aligned} E_1 &= \frac{H_0(estimated)}{H_0(true)} \\ &= \pi^{1/2} G(\beta) \frac{\theta_c}{\theta_0} \frac{g(0, 0, c_e, e_b, e_c, \theta, \phi)}{f^2(0, 0, c_e, e_b, e_c, \theta, \phi)}. \end{aligned} \quad (18)$$

Similarly, one can derive  $E_2 = H_0(estimated)/H_0(true)$  for the polytropic case, which is given by

$$\begin{aligned} E_2 &= \frac{H_0(estimated)}{H_0(true)} \\ &= \pi^{1/2} G(\beta) \frac{\theta_c}{\theta_0} \frac{g'(0, 0, c_e, e_b, e_c, \theta, \phi)}{f'^2(0, 0, c_e, e_b, e_c, \theta, \phi)} \left( \frac{T_{ew}}{T_{e0}} \right)^{\frac{3}{2}} \end{aligned} \quad (19)$$

where  $T_{ew}$  is the emission-weighted temperature, and the two functions  $f'$  and  $g'$  are defined as

$$f'(\theta_x/\theta_0, \theta_y/\theta_0, c_e, e_b, e_c, \theta, \phi) = \int \left\{ 1 - \frac{1}{K_0} \frac{\gamma - 1}{\gamma} [\Phi - \Phi_0] \right\}^{\frac{\gamma}{\gamma-1}} d(z'/R_0) \quad (20)$$

$$g'(\theta_x/\theta_0, \theta_y/\theta_0, c_e, e_b, e_c, \theta, \phi) = \int \left\{ 1 - \frac{1}{K_0} \frac{\gamma - 1}{\gamma} [\Phi - \Phi_0] \right\}^{\frac{\gamma+3}{2(\gamma-1)}} d(z'/R_0) \quad (21)$$

It is seen from eq.(18) and eq.(19) that the errors on  $H_0$  estimation depend on the mass distribution of clusters through  $\theta_0$ ,  $c_e$ ,  $e_b$ ,  $e_c$ , and on the equation of state of the intracluster gas. Furthermore, because of the asphericity of a cluster, different observing directions also give rise to different results. The parameters  $\theta_c$  and  $\beta$  are obtained by fitting the X-ray profile from the triaxial model with the  $\beta$ -model. Thus the values of  $\theta_c$  and  $\beta$  are dependent of the properties of clusters as well. Besides, because the 'true' X-ray profile for a triaxial cluster

does not follow the  $\beta$ -profile perfectly, the fitted  $\theta_c$  and  $\beta$  are affected by the maximum radius to which the fitting is applied (e.g., Navarro et al. 1995; Komatsu & Seljak 2001). It is noticed that  $E_1$  and  $E_2$  are very sensitive to the value of  $\beta$ . Figure 1 shows the function of  $G(\beta)$ . It is seen that with  $\beta < 0.5$ , the values of  $E_1$  and  $E_2$  can be very large. For the polytropic case, the region used to obtain the emission weighted temperature  $T_{ew}$  also matters in the estimation of  $H_0$ .

## 4. Results

In this section, we focus on the effects of the maximum fitting radius, the temperature gradient, and the polytropic index. We consider spherical clusters only. In the next section, we present our statistical analyses taking into account the asphericity of clusters.

Theoretically, both the spherical NFW model and the triaxial model assume an infinite extension of the mass distribution of dark matter halos. In reality however, an astrophysical object always has a finite size. In our following analysis, we cut the integration range in eq.(14) and eq.(15) at  $r_{int} = 5r_{vir}$ .

### 4.1. Effect of the maximum fitting radius

Because the X-ray emission depends on the square of the number density of electrons, it decreases sharply toward the outer part of a cluster. Thus in real observations, the fitting of the  $\beta$ -model to the X-ray profile is often performed in the inner part of a cluster where the signal-to-noise ratio is high enough. As we explained in the last section, different maximum fitting radii give rise to different values of  $\theta_c$  and  $\beta$ , and thus different estimates on the Hubble constant  $H_0$ .

Figure 2 shows the effects of  $r_{fit}$  on  $E_1$  and  $E_2$  for the isothermal and polytropic cases, respectively. The polytropic index  $\gamma$  is taken to be 1.15 in the case of  $E_2$ . It is noted that in the isothermal case, the Hubble constant  $H_0$  is systematically overestimated with the maximum deviation occurring at  $r_{fit} \sim 0.6r_{vir}$ . For clusters of  $M = 10^{14}h^{-1} M_\odot$ , the value of  $H_0(\textit{estimated})$  can deviate from the  $H_0(\textit{true})$  by as much as  $\sim 12\%$ . The deviations are larger for smaller clusters. For the polytropic gas, when  $r_{fit} \leq 0.2r_{vir}$ , an overestimation is observed and the deviations are larger for larger clusters. With  $r_{fit} > 0.2r_{vir}$ , the value of  $H_0$  is systematically underestimated with the maximum underestimation of  $\sim 12\%$  at  $r_{fit} \sim 0.6r_{vir}$ . The smaller the clusters are, the larger the underestimations are. In the following analyses, we will take  $r_{fit} = 0.6r_{vir}$ . For the NFW mass profile with  $\alpha = 1$ , the



mass within  $0.6r_{vir}$  is about  $0.7 M_{vir}$ , and the average density within it is therefore about  $3\rho_{vir} \approx 300\rho_{crit}$  at  $z = 0$  (e.g., Komatsu & Seljak 2001). Here  $\rho_{vir} = M_{vir}/(4\pi/3r_{vir}^3)$  and  $\rho_{crit}$  is the critical density of the universe.

## 4.2. Effect of the temperature gradient

When fitting the X-ray profile with the isothermal  $\beta$  model, the temperature used is the emission-weighted temperature  $T_{ew}$ . For the polytropic gas with a temperature distribution,  $T_{ew}$  is different from the central temperature  $T_{e0}$ , and thus the quantity  $(T_{ew}/T_{e0})^{3/2}$  in eq. (19) contributes an additional factor to  $E_2$ . It is clearly seen that  $T_{ew}$  depends on the temperature profile as well as on the region where the emission-weighted temperature is derived.

Given the temperature profile in the polytropic gas, we can calculate the emission-weighted temperature through the following equation (e.g., Ascasibar et al. 2003; Rasia et al. 2005)

$$T_{ew} \equiv \frac{\int n_e^2 T^{3/2} dV}{\int n_e^2 T^{1/2} dV}. \quad (22)$$

For a spherically symmetric gas distribution, the emission-weighted temperature can be written as

$$T_{ew} \equiv \frac{\int_0^{r_T} n_e^2 T^{3/2} r^2 dr}{\int_0^{r_T} n_e^2 T^{1/2} r^2 dr}. \quad (23)$$

Obviously,  $T_{ew}$  depends on the integral range  $r_T$ . Figure 3 shows the influence of  $r_T$  on the  $H_0$  estimation. In our calculations, we take  $\gamma = 1.15$ , and the  $\beta$  profile fitting is done out to a fixed radius of  $r_{fit} = 0.6r_{vir}$  when  $r_T$  is varying. When  $r_T$  is small,  $T_{ew}/T_{e0}$  is close to unity, and  $E_2 > 1$ . With  $r_T > 0.2r_{vir}$ ,  $E_2 < 1$  and reaches  $\sim 0.9$  as  $r_T \rightarrow r_{vir}$ . From Figure 3, it is seen that if we ignore the difference between  $T_{ew}$  and  $T_0$ , i.e., take  $T_{ew}/T_{e0} = 1$ ,  $E_2 > 1$ . Thus the underestimation appeared in the polytropic case is mainly due to  $T_{ew}/T_{e0} < 1$ . In the analyses presented in Figure 2 as well as in the following studies, we take  $r_T = 0.6r_{vir}$ .

## 4.3. The effect of the polytropic index

Given the mass distribution of a dark matter halo, both the density and the temperature profiles depend on the polytropic index  $\gamma$ . In this subsection, we discuss how  $\gamma$  affects the  $H_0$  estimation.

Figure 4 presents the dependence of  $E_2$  on  $\gamma$ . The fitting radii for the  $\beta$  profile and the emission-weighted temperature are  $r_{fit} = 0.6r_{vir}$  and  $r_T = 0.6r_{vir}$ , respectively. The mass of the cluster is  $M = 10^{14}h^{-1} M_\odot$ . The result shows that  $E_2 < 1$  when  $1.05 \leq \gamma \leq 1.4$ , and  $E_2 > 1$  when  $\gamma > 1.4$ . With  $\gamma$  approaching 1, the gas becomes isothermal and  $E_2$  reaches  $\sim 1.12$ , the result of  $E_1$  in Figure 2. At large  $\gamma$  with  $\gamma \sim 2$ , the value of  $E_2$  can be as high as about 1.6. We note that in the most theoretically probable range of  $\gamma \sim 1.15$  for the intracluster gas (Komatsu & Seljak 2001), the  $H_0$  is underestimated with the level of about 10%. Our results here are consistent with those of Puy et al. (2000) and Udomprasert et al. (2004)

Observationally, it is difficult to determine  $\gamma$  precisely. The available values of  $\gamma$  for clusters of galaxies are around  $\gamma \sim 1.2$  (e.g., Hughes et al. 1988; Finoguenov, Reiprich & Bohringer 2001; Pratt, Bohringer & Finoguenov 2005). Thus the polytropic index can be one of the factors that lead to the underestimation of  $H_0$  appeared in most of the observations.

## 5. Statistical analyses on the $H_0$ estimation in triaxial clusters

In this section, we discuss statistically the effects of the triaxiality of clusters on the  $H_0$  determination. Monte Carlo simulations are employed in the studies.

From eq.(18) and eq.(19), it is known that  $E_1$  and  $E_2$  depend on the mass distribution of dark matter halos through the concentration parameter  $c_e$ , and the eccentricities  $e_b$  and  $e_c$  (or equivalently the axial ratios  $b/a$  and  $c/a$ ), as well as on the observing direction  $(\theta, \phi)$ . It should be noted that the values of  $\beta, \theta_c$ , and  $T_{ew}/T_{e0}$  are also functions of  $(c_e, e_b, e_c, \theta, \phi)$ .

We first analyze the effects of line-of-sight directions. Given the mass configuration of a cluster, the probability function of  $E_1$  can be written as

$$F\left(E_1 \left| c_e, \frac{c}{b}, \frac{c}{a} \right.\right) = \frac{2}{\pi} \int_{\theta_1}^{\theta_2} \left( \frac{\partial E_1}{\partial \phi} \right)_{\theta, c_e, c/b, c/a}^{-1} \sin \theta d\theta, \quad (24)$$

where  $[\theta_1, \theta_2]$  is the integral range of  $\theta$  within which a physically meaningful value of  $\phi$  can be found for a given value of  $E_1$  (Binney & de Vaucouleurs 1981). The distribution function of  $E_2$  has the similar form. The results are presented in Figure 5. The top and bottom panels are for the isothermal and polytropic cases, respectively. The position of the vertical line in each plot indicates the peak value of  $E_1(E_2)$ . Two sets of  $(e_b, e_c)$  are considered. They are  $(e_b, e_c) = (0.2, 0.3)$  and  $(0.6, 0.8)$ . The corresponding axial ratios are  $(b/a, c/a) = (0.98, 0.95)$  and  $(0.8, 0.6)$ . In all the cases, the concentration parameter is taken to be the average one calculated from Jing and Suto (2002). The mass of the cluster is  $M = 10^{14}h^{-1} M_\odot$ . The redshift is  $z = 0.1$ . For the polytropic case, the value of  $\gamma$  is taken to be 1.15.

With small  $e_b$  and  $e_c$  (left panels), the distribution functions of  $E_1$  and  $E_2$  are peaked at  $\sim 1.1$  and  $\sim 0.9$  with narrow extensions, respectively. For the isothermal case, the distribution concentrates on the side of  $E_1 > 1$ . For the polytropic case, the distribution is on the side of  $E_2 < 1$ . Because of the small asphericity, the results are similar to those of the spherical cases presented in Figure 2 with  $r_{fit} = 0.6r_{vir}$ . It is known that the combined analysis of X-ray and SZ effects of a cluster leads directly to an estimate on the line-of-sight dimension of the cluster. With an observed angular extension of the cluster, the angular diameter distance to the cluster is determined by assuming the equality of the sizes of the cluster parallel and perpendicular to the line of sight. Thus for a triaxial cluster oriented with its long axis along the line of sight, one may expect an overestimation for the angular diameter distance, and therefore an underestimation for  $H_0$ . The reverse trend is expected for a cluster with its short axis along the line of sight. Thus it seems that the distribution should extend to both  $E_1(E_2) > 1$  and  $E_1(E_2) < 1$ , which is not seen in the left panels of Figure 5. The reason for this is that the above qualitative analysis considers only the effect of the asphericity. Taking into account the errors introduced by the differences between the real gas distribution and that of the isothermal  $\beta$  model, the peak values of  $E_1$  and  $E_2$  shift away from unity.

With the increase of the asphericity, the distributions become broader. For the polytropic case with  $(e_b, e_c) = (0.6, 0.8)$ , the values of  $E_2$  move to the side of  $E_2 > 1$ . The peak value of  $E_2$  is around 1.8. This large overestimation is mainly due to the small  $\beta$  value obtained by fitting the strongly triaxial and polytropic gas distribution to the isothermal  $\beta$  model.

Now the distributions of  $E_1$  and  $E_2$  are investigated taking into the statistics of  $c_e$ ,  $e_b$  and  $e_c$ . For a sample of clusters with a given mass  $M$  and at a redshift  $z$ , we have, for the isothermal case,

$$F(E_1|M, z)dE_1 = \left[ \frac{2}{\pi} \int p\left(\frac{c}{a}\right)d\left(\frac{c}{a}\right) \int p\left(\frac{c}{b}\middle|\frac{c}{a}\right)d\left(\frac{c}{b}\right) \int p(c_e)dc_e \int \left(\frac{\partial E_1}{\partial \phi}\right)_{\theta, c_e, c/b, c/a}^{-1} \sin \theta d\theta \right] dE_1, \quad (25)$$

where the distributions of  $c_e$ ,  $c/b$  and  $c/a$  are taken from Jing and Suto (2002) (Wang & Fan 2004). For the polytropic case, the distribution of  $E_2$  has the similar form.

Figure 6 shows the results for different  $\gamma$ . The cluster mass  $M = 10^{14}h^{-1} M_\odot$  and  $z = 0.1$ . A clear trend is observed. As the value of  $\gamma$  increases, the distribution extends more toward high  $E_2$ . With  $\gamma = 1.2$ , the tail goes well beyond  $E_2 = 3$ . The position of the vertical line in each panel indicates the peak value of  $E_1(E_2)$ . The symbols represent the average values of  $E_1(E_2)$ . In Figure 7, we show explicitly the change of the average value of  $E_2$  with  $\gamma$ . For the isothermal case with  $\gamma = 1$ ,  $E_1^{ave} \sim 1.06$ . For the case with  $\gamma = 1.15$ ,  $E_2^{ave} \sim 3$ . It is reminded that our previous analysis on the spherical clusters with

$\gamma = 1.15$  gives the result of  $E_2 \sim 0.9$  (Figure 2). Thus the asphericity strongly influences the determination of  $H_0$  in the polytropic case due to the small fitted value of  $\beta$ .

We present the results for clusters with different  $M$  at different  $z$  in Figure 8. The positions of the vertical lines represent the peak values of  $E_1(E_2)$ . The numbers in the parentheses are the average values of  $E_1(E_2)$ . For the isothermal case with  $z = 0.1$ , the average value of  $E_1$  is 1.05, 1.06 and 1.08 for  $M = 10^{13}h^{-1} M_\odot$ ,  $10^{14}h^{-1} M_\odot$ , and  $10^{15}h^{-1} M_\odot$ , respectively. For  $M = 10^{14}h^{-1} M_\odot$ , the values of  $E_1^{ave}$  at  $z = 0.1, 0.5$  and  $0.9$  are respectively 1.06, 1.08 and 1.2. In these distributions, the peak value of  $E_1$  is around 1.05. In the case of polytropic gas with  $\gamma = 1.15$  and  $z = 0.1$ , we have  $E_2^{ave} = 2.6, 3.0$  and  $3.5$  for  $M = 10^{13}h^{-1} M_\odot$ ,  $10^{14}h^{-1} M_\odot$ , and  $10^{15}h^{-1} M_\odot$ , respectively. The corresponding peak values are 1.05, 1.35, and 1.35. With a fixed mass of  $M = 10^{14}h^{-1} M_\odot$ , the peak values of  $E_2$  are 1.35, 1.55, and 1.55 for  $z = 0.1, 0.5$  and  $0.9$ , respectively. The respective average values of  $E_2$  are 3.0, 3.6 and 6.1. Thus for massive clusters at relatively high redshifts, the errors in  $H_0$  determination are large due to their strong asphericities. Observationally, however, high redshift clusters with strongly distorted X-ray/SZ images are usually not used in the determination of the angular diameter distance because very likely they are still in the merging stage.

We further study statistically the errors for a mass-limited cluster sample with  $M_{lim} = 10^{13}h^{-1} M_\odot$ . The probability function for  $E_1$  ( $E_2$ ) has the following form (Wang & Fan 2004)

$$F(E_1) = \frac{\int dV(z) \int_{M_{lim}} F(E_1|M, z)(dn/dM)dM}{\int (dn/dM)dMdV}, \quad (26)$$

where  $F(E_1|M, z)$  is the probability density of  $E_1$  for clusters of mass  $M$  and at redshift  $z$ ,  $(dn/dM)dM$  is the number density of clusters in the mass range of  $(M, M + dM)$ , and  $dV$  is the volume element. The redshift range is taken to be  $z = [0, 1]$ . The number density of clusters is modeled based on the analyses of Jenkins et al. (2001). The results are shown in Figure 9. For the isothermal case, the distribution is peaked at  $E_1 \sim 1$  and  $E_1^{ave} \approx 1.06$  with a dispersion about  $\pm 20\%$ . For the polytropic case with  $\gamma = 1.15$ , the distribution function has a peak at  $E_2 \approx 1.37$  and a long tail extending to high  $E_2$  values. The average value of  $E_2$  is  $E_2^{ave} \approx 3$ . Thus for a mass-limited sample of clusters, the  $H_0$  estimation can be highly biased due to the combined effects of non-isothermality and asphericities.

There have been different studies on the systematics involved in  $H_0$  determination (e.g., Sulkanen 1999; Udomprasert et al. 2004). With numerical simulations, two groups recently analyzed possible errors in estimating  $H_0$  (Ameglio et al. 2005; Hallman et al. 2005). While both of them noted the significant effects of the non-isothermality, they found opposite tendencies in the  $H_0$  determination. Ameglio et al. (2005) presented an overestimation on  $H_0$ , while an underestimation on  $H_0$  was reported in Hallman et al. (2005). Our analyses

for the spherical case show a  $\sim 15\%$  underestimation in  $H_0$  with  $\gamma$  in the range of 1.05 to 1.4. The bias becomes positive for larger  $\gamma$  (see Figure 4). Including the triaxiality of clusters, however, we find a very large bias toward overestimation in  $H_0$  with  $E_2^{ave} \sim 3$  for  $\gamma = 1.15$ . The differences in the results from different groups are associated with different gas distributions and temperature profiles adopted in the analyses. While both Ameglio et al. (2005) and Hallman et al. (2005) rely on numerical simulations, we derive the properties of the intracluster gas from the triaxial mass distribution of dark matter halos under the approximation of hydrodynamic equilibrium. Even both from simulations, the obtained mass and temperature distributions of the intracluster gas can be quite different from one group to another because of the differences existed in modeling processes. It is also noted that in Ameglio et al. (2005), just as we have done in this paper, the parameters  $\beta$  and  $\theta_c$  were determined by fitting the  $\beta$  model to the X-ray images alone. Hallman et al. (2005), on the other hand, obtained the fitting parameters from X-ray and SZ images. This difference in the fitting technique can be an important reason to account for the different results shown by the two groups. The large dispersion appeared in different analyses indicates that the error analysis itself is model dependent. Different analyzing procedures can also lead to different conclusions. In our analyses, each time we change the properties of the intracluster gas, we obtain a new set of fitting values for  $\beta$  and  $\theta_c$ . Some other studies may fix the values of  $\beta$  and  $\theta_c$  while changing the intrinsic gas properties (e.g., Udomprasert et al. 2004).

Confronted with observations, the large positive bias shown in the above studies for the polytropic gas has not been seen in observational analyses. Most of the results on  $H_0$  derived from joint X-ray and SZ observations are biased low in comparison with that determined from other observations (e.g., Reese et al. 2002; Freedman et al. 2001), although for a couple of clusters the estimated values of  $H_0$  are as high as about 100 km/s/Mpc (e.g., Mason et al. 2001, Jones et al. 2003). There are several issues that might be related to this apparent discrepancy.

In our studies, we assume that there are no correlations between the polytropic index  $\gamma$  and the triaxiality of clusters ( $e_b, e_c$ ). Thus, for each  $\gamma$ , the analyses are performed for a full sample of clusters with the statistics of the triaxiality given by Jing and Suto (2002). It is unclear, however, if  $\gamma$  and ( $e_b, e_c$ ) are associated with each other. In Figure 10, we plot the measured  $\gamma$  and axial ratios  $\eta$  of the X-ray profiles for clusters of galaxies collected from literatures. Keeping in mind the large error bars, we see a tendency that high  $\gamma$  is likely related with small  $\eta$ , i.e., clusters with higher  $\gamma$  tend to be more spherical. If the correlations indeed exist, the bias for polytropic and triaxial clusters can be overestimated (comparing Figure 7 with Figure 4). With numerical simulations, it is readily testable if there are any relations between  $\gamma$  and the shape of the gas distribution.

Another issue is related to the  $\beta$  value, to which the bias is very sensitive. It is noted that for observed clusters, most of the  $\beta$  values are in the range of  $[0.5, 0.8]$ . Considering only the subsample of clusters with  $\beta = [0.5, 0.8]$ , our analysis gives  $E_1 \approx 1.002$  and  $E_2 \approx 0.994$ .

Observationally, clusters with strongly aspherical X-ray/SZ profiles are often avoided to be used in the  $H_0$  measurement. Here we study the effects of these highly elongated clusters on the statistical result of  $H_0$  for the sample of clusters with  $M = 10^{14}h^{-1} M_\odot$ ,  $z = 0.1$  and  $\gamma = 1.15$ . In Figure 11, we show the distributions of  $E_2$  for the full sample (solid line), for the subsample with  $\eta \geq 0.95$  (dotted line) and for the subsample with  $\beta \geq 0.5$  (dash-dotted line). Here  $\eta$  is the axial ratio of the X-ray isophote contour at the virial radius of a cluster. It is seen that the distribution of the subsample with  $\eta \geq 0.95$  indeed shifts toward small  $E_2$  but not significantly in comparison with that of the full sample. We have  $E_2^{peak}(\eta \geq 0.95) \approx 1.25$  and  $E_2^{ave}(\eta \geq 0.95) \approx 2.5$ . For the full sample, the values are  $E_2^{peak} \approx 1.35$  and  $E_2^{ave} \approx 3.0$ . For the subsample with  $\beta \geq 0.5$ , however, the distribution of  $E_2$  is narrowly around  $E_2 \sim 1$ . We therefore immediately see that  $E_2$  depends dominantly on the value of  $\beta$ , and the long tail in the distribution of the full sample is resulted from small values of  $\beta$ . On the other hand, limiting  $\eta$  cannot significantly affect the  $E_2$  distribution. The apparent reason for this is that for a given  $\eta$ , a range of  $\beta$  values can exist as shown in Figure 12, where we apply a cut on  $\beta \geq 0.33$ . For each  $\eta$ , the maximum  $\beta$  value is highly correlated with the value of  $\eta$ , but the scatter plot shows a large extension toward small  $\beta$ . The existence of these small  $\beta$  values results the long tail in the  $E_2$  distribution for the subsample with  $\eta \geq 0.95$ . We further analyze the correlations of  $\eta$  and  $\beta$  with the intrinsic asphericity of dark matter halos represented by  $e_b$  and  $e_c$ . In Figure 13, we plot the distributions of  $e_b$  and  $e_c$  for the three samples respectively. Clusters in the subsample with  $\beta \geq 0.5$  are apparently biased toward spherical ones in comparison with the full sample. For the subsample with  $\eta \geq 0.95$ , however, the distributions of  $e_b$  and  $e_c$  shift only slightly to smaller values of  $e_b$  and  $e_c$ . Thus the value of  $\beta$  is more sensitive to  $e_b$  and  $e_c$  than  $\eta$  is. In Wang and Fan (2004), we analyze the dependence of  $\eta$  on the intrinsic mass distribution of dark matter halos. Because the distribution of the intracluster gas follows directly the profile of the gravitational potential, it is more spherical than the distribution of the dark matter is. Moreover, the shapes of X-ray/SZ images also depend on line-of-sight directions. The resulting  $\eta$  for the full sample of clusters discussed here is peaked around  $\eta \sim 0.9$ . In other words, while clusters with highly distorted X-ray/SZ images (small  $\eta$ ) are strongly aspherical intrinsically, samples with nearly circular images (large  $\eta$ ) can still contain clusters with high values of  $(e_b, e_c)$ . On the other hand, we find that the radial distribution of the intracluster gas is very sensitive to the intrinsic asphericity of the dark matter distribution, and thus the fitted  $\beta$  value is sensitive to  $(e_b, e_c)$ . Clusters with larger values of  $(e_b, e_c)$  tend to have flatter distributions of the intracluster gas, and therefore smaller  $\beta$  values. In Figure 14, we show

the circularized radial profiles of the X-ray surface brightness for three specific clusters all with  $\eta = 0.95$ . Fitting the profiles with the isothermal  $\beta$ -model, we get  $\beta = 0.4, 0.5$ , and  $0.6$ , respectively. The respective  $(e_b, e_c)$  of underlying dark matter distributions are  $(0.67, 0.77)$ ,  $(0.48, 0.71)$  and  $(0.40, 0.54)$ . Combining the results shown in Figure 11 and Figure 13, we conclude that by considering intrinsically nearly spherical clusters only, we eliminate the large overestimates on  $H_0$ . The  $\beta$  value is a better indicator of the asphericity of underlying dark matter distribution than the two-dimensional axial ratio of X-ray/SZ isophote contours  $\eta$  is. Our study presented here also opens a possibility of using the distribution of the  $\beta$  value to probe statistically the intrinsic mass distribution of dark matter halos.

There are other physical factors that can affect the  $H_0$  determination considerably. Analyses based on numerical simulations show that (e.g., Ameglio et al. 2005) excluding unrelaxed clusters with apparent substructures from a sample of clusters can significantly reduce the errors in the  $H_0$  estimation. The intrinsic anisotropies of CMB can also introduce a notable bias on the  $H_0$  determination (e.g., Udomprasert et al. 2004).

## 6. Summary and Discussion

Combined analyses of X-ray and SZ effect observations provide an important means in determining the angular diameter distances to clusters of galaxies. In comparison with the method using standard candles, this determination does not depend on distance ladders, and thus avoids the error propagation from ladder to ladder. Furthermore, the X-ray/SZ observations and observations on standard candles involve different systematic errors. Therefore important tests on the consistency of cosmological theories can be possible by comparing the results on the evolution of the universe from two sets of observations. Besides the determination on  $H_0$ , observations on high-redshift clusters can lead to a Hubble diagram of  $D_A - z$  relation, which potentially can be used to constrain cosmological parameters just as SNe Ia observations do. In order to extract useful cosmological information, however, one needs to understand thoroughly the systematic errors involved in the method of X-ray/SZ observations.

In this paper, we focus on the triaxiality and non-isothermality of clusters of galaxies. From the triaxial model of dark matter halos (Jing & Suto 2002), the equilibrium distribution of the intracluster gas is derived, which is generally aspherical and non-isothermal. The systematic errors in  $H_0$  estimation are evaluated with Monte Carlo simulations.

Our main results can be summarized as follows:

- (i) Different extension adopted in fitting the  $\beta$ -model to the profile of X-ray emissions

can introduce as much as about 12% bias in the estimated  $H_0$  value for  $M = 10^{14}h^{-1} M_\odot$ . For the isothermal case, the bias is an overestimate, while it is an underestimate for the polytropic gas with  $r_{fit} > 0.3r_{vir}$ .

(ii) The maximum radius  $r_T$  used to calculate the emission-weighted temperature in the polytropic case can affect  $H_0$  considerably. With  $r_T \leq 0.2r_{vir}$ , the value of  $H_0$  is overestimated. At larger  $r_T$ , it is underestimated by about 10% with  $\gamma = 1.15$ .

(iii) In the spherical case, the effect of the non-isothermality depends on the polytropic index  $\gamma$ . With  $1.05 \leq \gamma \leq 1.4$ ,  $H_0$  can be underestimated by nearly 20%. A larger  $\gamma$  gives rise to a positive bias. As  $\gamma$  is close to the adiabatic value of 1.7, the overestimate is about 10%.

(iv) With the increase of the asphericity of clusters, the scatters in the estimated  $H_0$  become large. Meanwhile, the peak value of  $H_0$  changes significantly. For the polytropic case with  $\gamma = 1.15$ , the peak  $H_0$  changes from  $H_0^{peak}(estimated) \approx 0.9H_0(true)$  to  $H_0^{peak}(estimated) \approx 1.8H_0(true)$  as  $(e_b, e_c)$  increases from (0.2, 0.3) to (0.6, 0.8). The average  $H_0^{ave}(estimated)$  for a sample of clusters with a given mass  $M$  and at a redshift  $z$  is very sensitive to  $\gamma$ . For  $M = 10^{14}h^{-1} M_\odot$  and  $z = 0.1$ ,  $H_0^{ave}(estimated) \approx 1.7H_0(true)$  at  $\gamma = 1.05$ , and at  $\gamma = 1.2$ ,  $H_0^{ave}(estimated) \approx 3.6H_0(true)$ . Because the asphericities of clusters increase with their masses and redshifts (Jing & Suto 2002), the bias on  $H_0$  increases with  $M$  and  $z$  as well.

(v) For a mass-limited sample of clusters with  $M = 10^{13}h^{-1} M_\odot$ , we have  $H_0^{ave}(estimated) \approx 1.06H_0(true)$  and the scatters are around  $\pm 20\%$  for the isothermal case. For the polytropic case with  $\gamma = 1.15$ , the peak value of  $H_0^{peak}(estimated)$  is about  $1.4H_0(true)$ . There is a very extended tail toward high  $H_0(estimated)$ , which results an average value of  $H_0^{ave}(estimated) \approx 3H_0(true)$ .

(vi) For  $M = 10^{14}h^{-1} M_\odot$ ,  $z = 0.1$ , and  $\gamma = 1.15$ , we analyze statistically the errors for different subsamples of clusters. For the subsample of clusters with  $\beta$  being in the range of [0.5, 0.8], which is the range for most observed clusters, the average value of the estimated  $H_0$  is about  $1.002H_0(true)$  and  $0.994H_0(true)$  for the isothermal and polytropic cases, respectively. We also consider a subsample of clusters with nearly circular X-ray images. Specifically, we select clusters with the axial ratio of two-dimensional X-ray images  $\eta \geq 0.95$ . The distribution of  $E_2$  for this subsample of clusters shifts to smaller  $E_2$  side in comparison with the full sample. But there is still a long tail toward high values of  $E_2$ . On the other hand, for clusters with  $\beta \geq 0.5$ , the estimated  $E_2$  are around  $E_2 \sim 1$  with  $\pm 10\%$  scatters. We further show that the  $\beta$ -limited sample is clearly biased more to intrinsically spherical ones than the  $\eta$ -limited sample is. Thus by limiting the value of  $\beta \geq 0.5$ , we



essentially select clusters that are nearly spherical intrinsically. For these clusters, we can obtain a fair estimate on  $H_0$  through joint X-ray/SZ analyses.

Based on the triaxial model of dark matter halos, our analyses avoid ad hoc assumptions on the aspherical distribution of the intracluster gas. On the other hand, the condition of the hydrodynamic equilibrium used in our study is likely a simplification. The real gas distribution and the temperature profile of a cluster of galaxies can be more complex than our model can describe (e.g., Kempner et al. 2002; O’Hara et al. 2004; Reiprich et al. 2004; Inagaki et al. 1995; De Grandi & Molendi 2002). With dramatic advances in both X-ray and SZ observations, however, the knowledge on the intracluster gas will improve greatly. It is becoming possible observationally to describe the intracluster gas more precisely than the isothermal  $\beta$ -model does. Therefore better determinations on  $H_0$  and even other cosmological parameters are highly expected from analyses on clusters of galaxies.

We are very grateful for the referee’s encouraging and constructive comments and suggestions. This research was supported in part by the National Science Foundation of China under grants 10243006 and 10373001, by the Ministry of Science and Technology of China under grant TG1999075401, by the Key Grant Project of Chinese Ministry of Education (No. 305001), and by the National Science Foundation of China under grant 10533010.

## REFERENCES

- Ameglio, S., Borgani, S., Diaferio, A., & Dolag, K. 2005, astro-ph/0510797
- Andreani, P. et al. 1999, ApJ, 513, 23
- Ascasibar, Y., Yepes, G., Müller, V., & Gottlöber, S. 2003, MNRAS, 346, 731
- Belsole, E., Sauvageot, J. L., & Pratt, G. W., & Bourdin, H. 2005, A&A, 430, 385
- Binney, J., & de Vaucouleurs, G. 1981, MNRAS, 194, 679
- Birkinshaw, M., & Hughes, J. P. 1994, ApJ, 420, 33
- Birkinshaw, M., Hughes, J. P., & Arnaud, K. A. 1991, ApJ, 379, 466
- Birkinshaw, M., & Hughes, J. P. 1994, ApJ, 420, 33
- Carlstrom, J. E., Holder, G. P., & Reese, E. D. 2002, ARA&A, 40, 643
- Cooray, A. R. 1998, A&A, 339, 623

- De Filippis, E., Sereno, M., Bautz, M. W., & Longo, G. 2005, *ApJ*, 625, 108
- De Grandi, S., & Molendi, S. 2002, *ApJ*, 567, 163
- Finoguenov, A., Reiprich, T. H., & Böhringer, H. 2001, *A&A*, 368, 749
- Freedman, W. L., et al. 2001, *ApJ*, 553, 47
- Hallman, E. J., Burns, J. O., Motl, P. M., & Norman, M. L. 2005, *adtro-ph/0510745*
- Hubble, E. P. 1929, *Proc. Natl. Acad. Sci.*, 15, 168
- Hughes, J. P., & Birkinshaw, M. 1998, *ApJ*, 501, 1
- Hughes, J. P., Yamashita, K., Okumura, Y., Tsunemi, H., & Matsuoka, M. 1988, *ApJ*, 327, 615
- Inagaki, Y., Suginozaka, T., & Suto, Y. 1995, *PASJ*, 47, 411
- Jenkins, A., et al. 2001, *MNRAS*, 321, 372
- Jing, Y. P., & Suto, Y. 2002, *ApJ*, 574, 538
- Jones, M. et al. 1993, *Nature*, 365, 320
- Jones, M. E., et al. 2003, *MNRAS*, submitted (*astro-ph/0103046*)
- Keeton, C. R., & Zabludoff, A. I. 2004, *ApJ*, 612, 660
- Kempner, J. C., Sarazin, C. L., & Ricker, P. M. 2002, *ApJ*, 579, 236
- Komatsu, E., & Seljak, U. 2001, *MNRAS*, 327, 1353
- Lee, J., & Suto, Y. 2003, *ApJ*, 585, 151
- Lee, J., & Suto, Y. 2004, *ApJ*, 601, 599
- Markevitch, M., Vikhlinin, A., Forman, W. R., & Sarazin, C. L. 1999, *ApJ*, 527, 545
- Mason, B. S., Myers, S. T., & Readhead, A. C. S. 2001, *ApJ*, 555, L11
- McHardy, I. M., Stewart, G. C., Edge, A. C., Cooke, B., Yamashita, K., & Hatsukade, I. 1990, *MNRAS*, 242, 215
- Mohr, J. J., Evrard, A. E., Fabricant, D. G., & Geller M. J. 1995, *ApJ*, 447, 8
- Navarro, J. F., Frenk, C. S., & White, S. D. M. 1995, *MNRAS*, 275, 720

- Oguri, M., & Keeton, C. R. 2004, *ApJ*, 610, 663
- Oguri, M., Lee, J., & Suto, Y. 2003, *ApJ*, 599, 7
- O’Hara, T. B., Mohr, J. J., & Guerrero, M. A. 2004, *ApJ*, 604, 604
- Perlmutter, S., Turner, M. S., & White, M. 1999, *Phys. Rev. Lett*, 83, 670
- Pratt, G. W., Böhringer, H., & Finoguenov, A. 2005, *A&A*, 433, 777
- Puy, D., Grenacher, L., Jetzer, Ph., & Signore, M. 2000, *A&A*, 363, 415
- Rasia, E., et al. 2005, *ApJ*, 618, 1L
- Reese, E. D. 2004, in “Measuring and Modeling the Universe”, ed.: W. L. Freedman, Carnegie Observatories Astrophysics Series, Volume 2, Cambridge University Press, Cambridge, 138
- Reese, E. D., Carlstrom, J. E., Joy, M., Mohr, J. J., Grego, L., & Holzzapfel, W. L. 2002, *ApJ*, 581, 53
- Reiprich, T. H., Sarazin, C. L., Kempner, J. C., & Tittley, E. 2004, *ApJ*, 608, 179
- Riess, A. G., et al. 1998, *AJ*, 116, 1009
- Roettiger, K., Stone, J. M., & Mushotzky, R. F. 1997, *ApJ*, 482, 588
- Rosati, P., Borgani, S., & Norman, C. 2002, *ARA&A*, 40, 539
- Schmidt, R. W., Allen, S. W., & Fabian, A. C. 2004, *MNRAS*, 352, 1413
- Sulkanen, M. E. 1999, *ApJ*, 522, 59
- Sunyaev, R. A., & Zel’dovich, Y. B. 1970, *Comments Astrophys. Space Phys.*, 2, 26
- Sunyaev, R. A., & Zel’dovich, Y. B. 1972, *Comments Astrophys. Space Phys.*, 4, 173
- Tang, J. Y., & Fan, Z. H. 2005, *ApJ*, 635, 60
- Udomprasert, P. S., Mason, B. S., Readhead, A. C. S., & Pearson, T. J. 2004, *ApJ*, 615, 63
- Wang, Y. -G., & Fan, Z. -H. 2004, *ApJ*, 617, 847

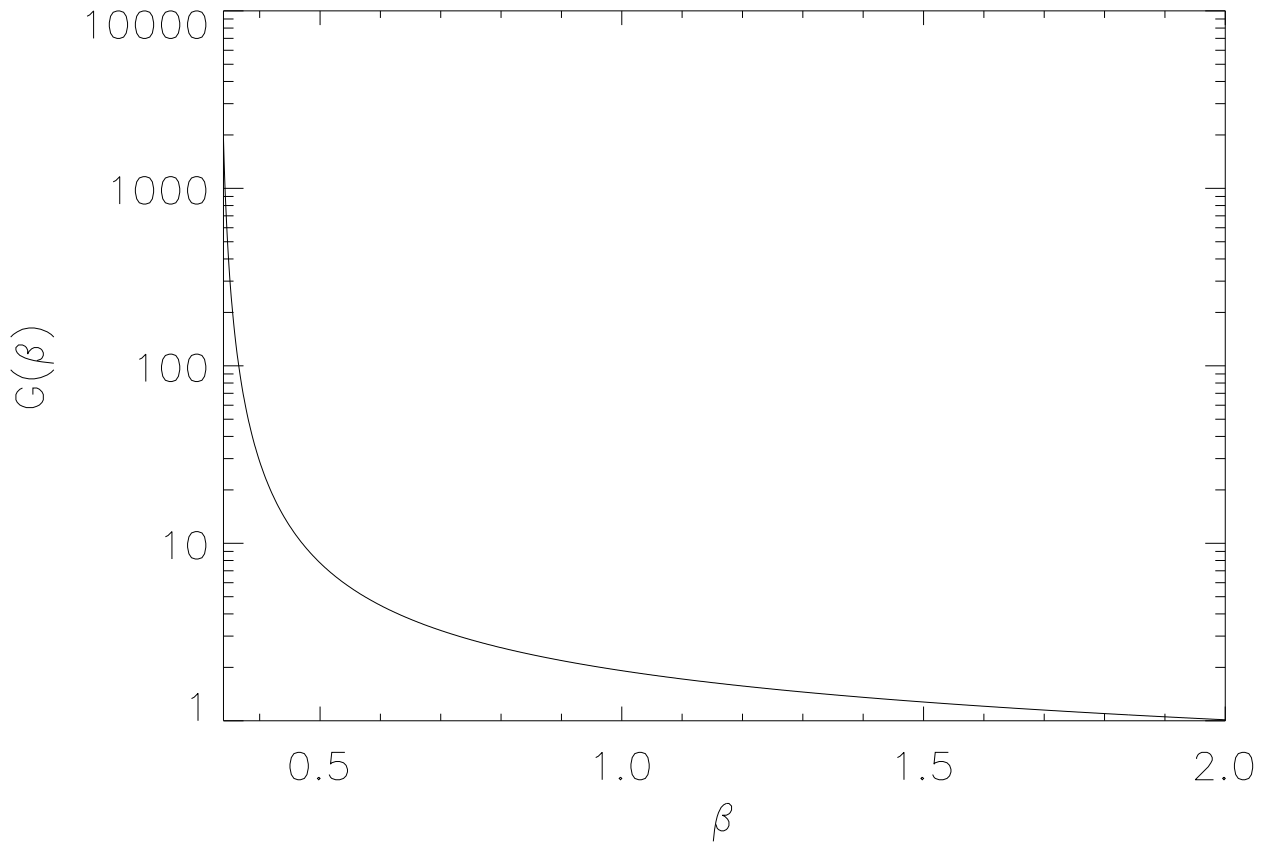


Fig. 1.— The dependence of  $G(\beta)$  on  $\beta$ .

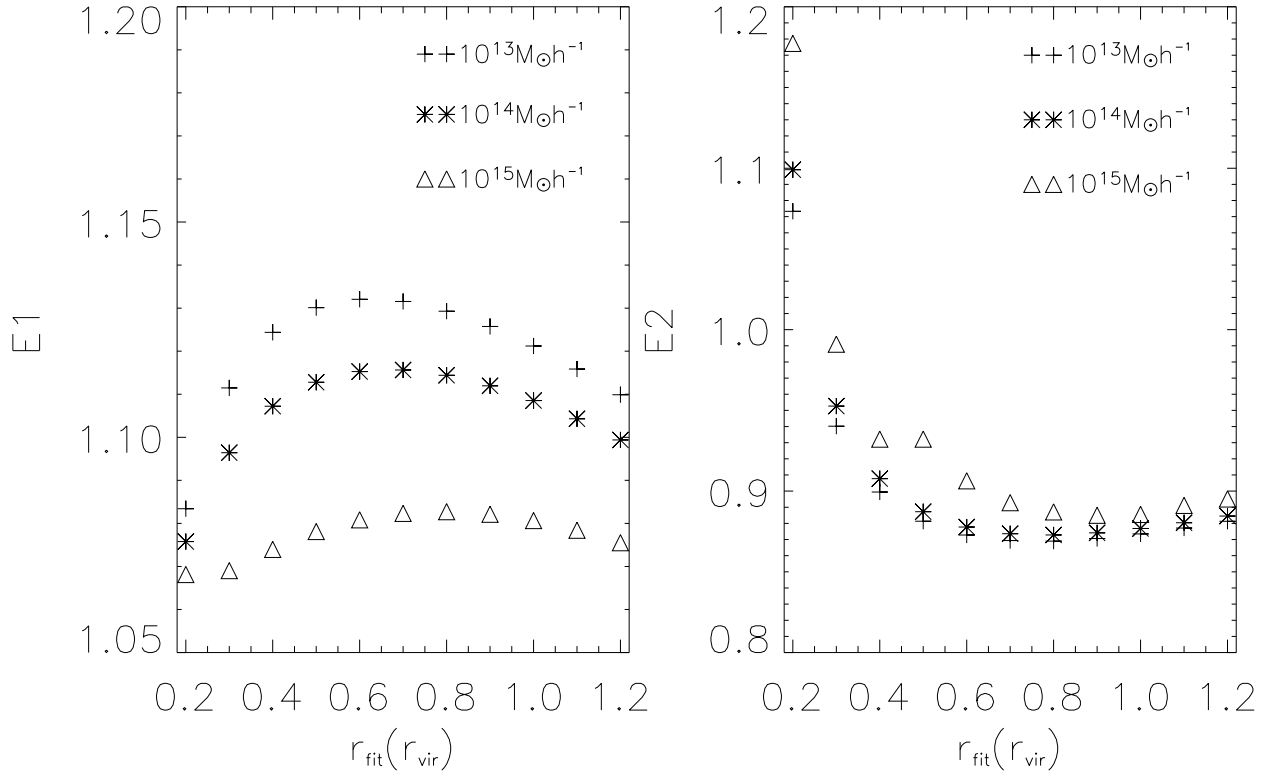


Fig. 2.— The dependence of  $E_1$  and  $E_2$  on the maximum fitting radius  $r_{fit}$ . Spherical clusters are considered. The left panel is for the isothermal case, and the right panel is the polytropic case with  $\gamma = 1.15$ . The pluses, asterisks and triangles are for  $M = 10^{13} h^{-1} M_{\odot}$ ,  $10^{14} h^{-1} M_{\odot}$  and  $10^{15} h^{-1} M_{\odot}$ , respectively.

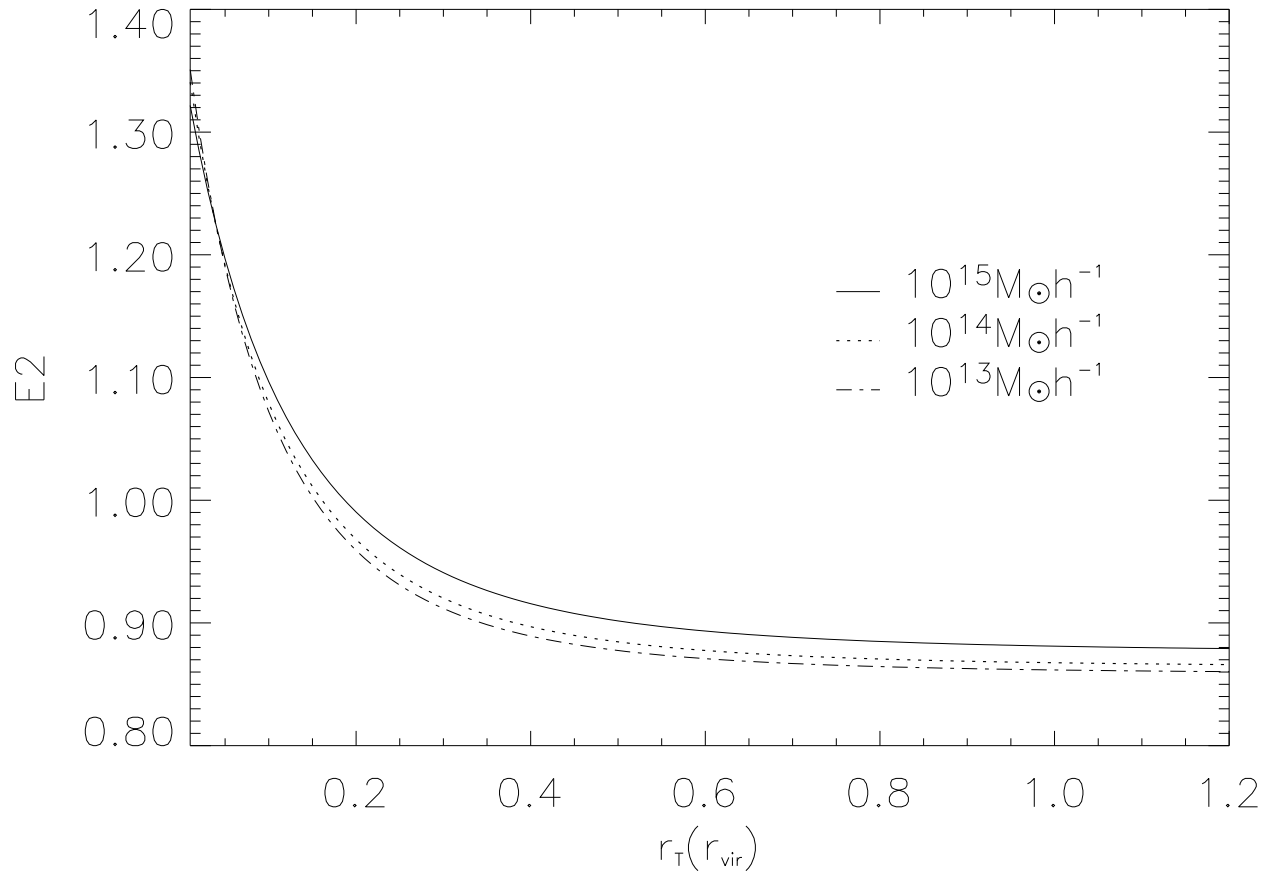


Fig. 3.— Influence of  $r_T$  on  $E_2$ . Spherical clusters are considered, and the polytropic index  $\gamma$  is taken to be 1.15. The solid, dotted, and dash-dotted lines are for  $10^{15} h^{-1} M_{\odot}$ ,  $10^{14} h^{-1} M_{\odot}$ , and  $10^{13} h^{-1} M_{\odot}$ , respectively.

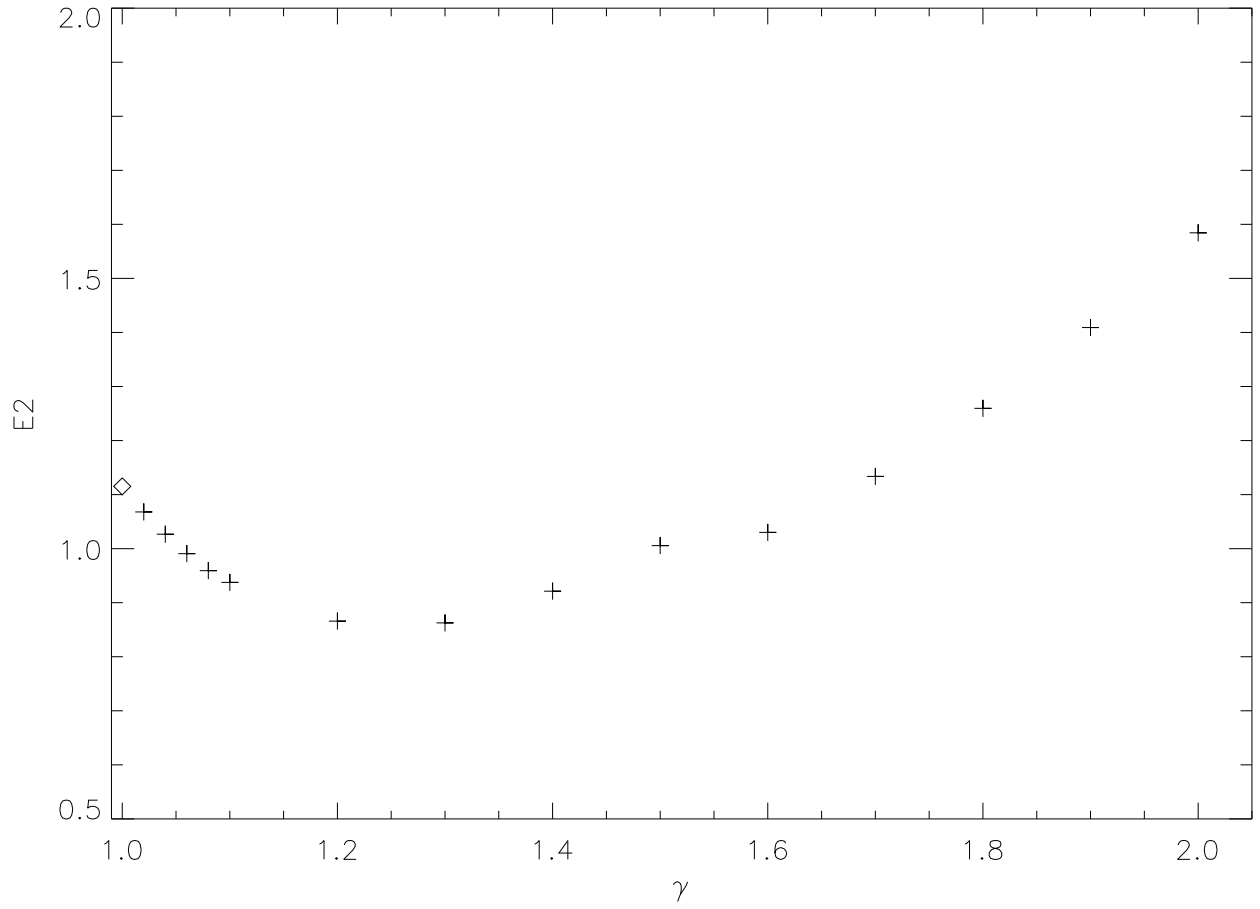


Fig. 4.— The dependence of  $E_2$  on  $\gamma$ . Spherical clusters are considered and the mass is taken to be  $10^{14}h^{-1}M_{\odot}$ .

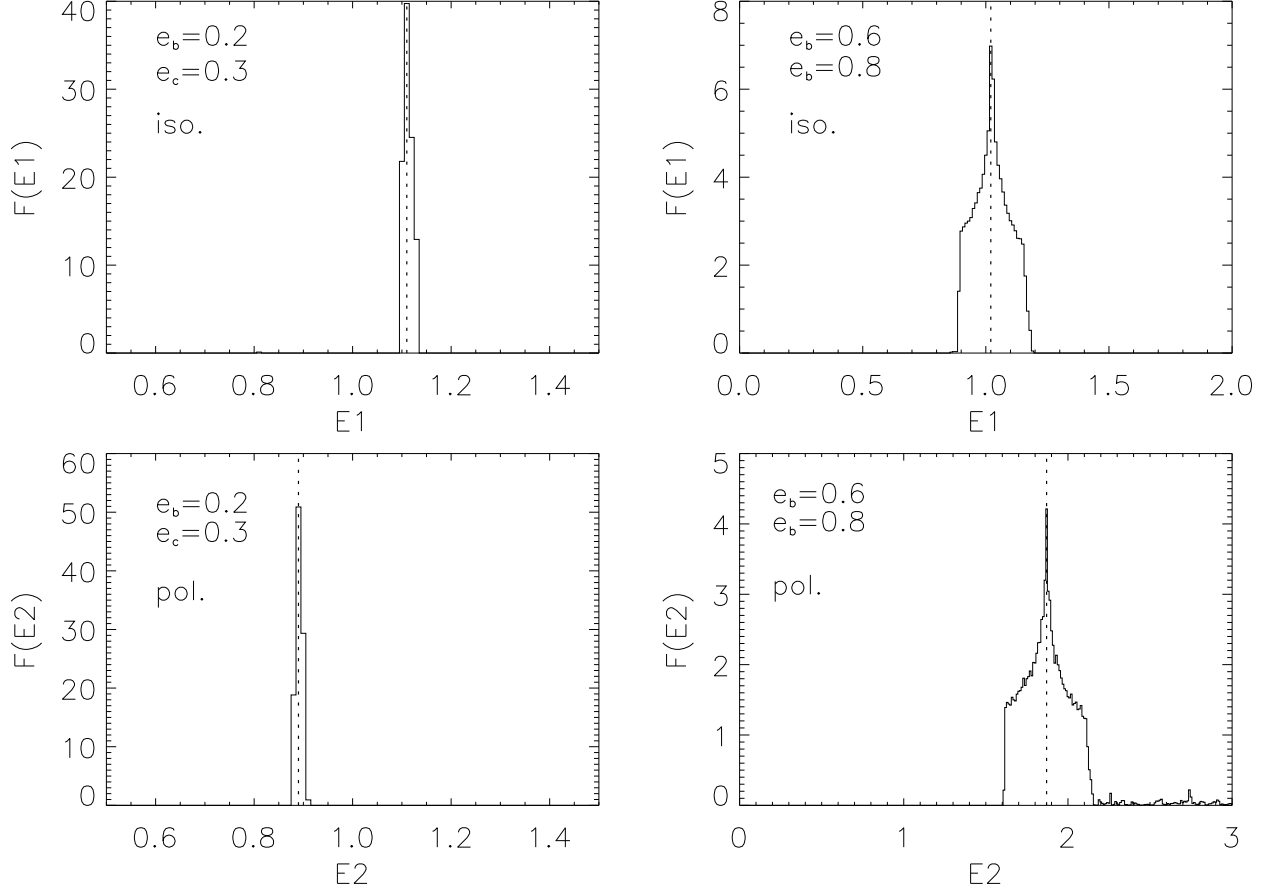


Fig. 5.— Conditional probabilities  $F(E_1|c_e, c/b, c/a)$  and  $F(E_2|c_e, c/b, c/a)$  for clusters with  $M = 10^{14}h^{-1}M_\odot$  and  $z = 0.1$ . The top and bottom panels show the isothermal and polytropic cases, respectively. The vertical lines indicate the peak values of  $E_1(E_2)$ .



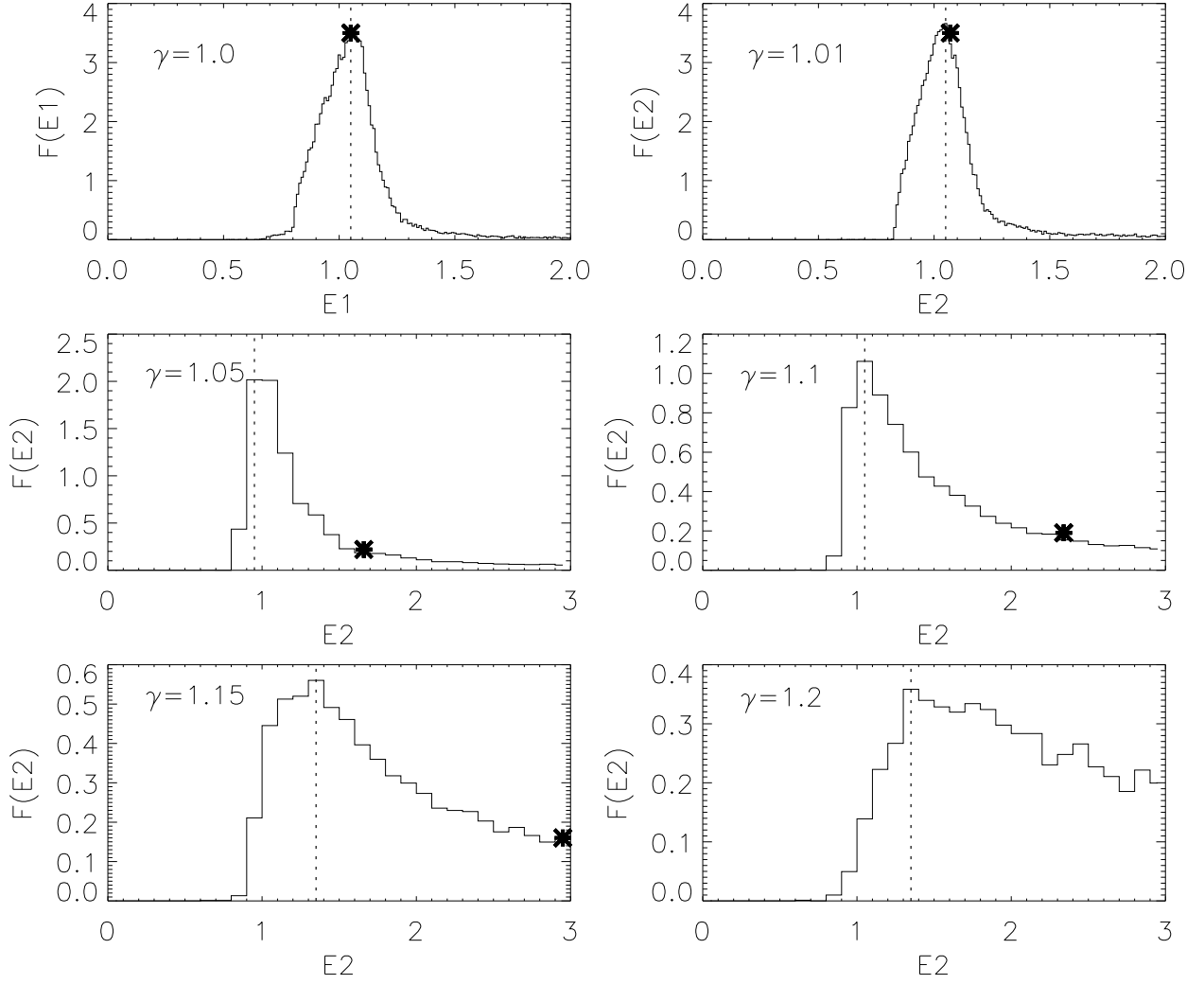


Fig. 6.— Probability functions  $F(E_1|M, z)$  (top left panel) and  $F(E_2|M, z)$  with  $M = 10^{14}h^{-1}M_\odot$  and redshift  $z = 0.1$ . In each panel, the peak value of  $E_1$  ( $E_2$ ) is indicated by the vertical line. The symbols show the average values of  $E_1$  ( $E_2$ ).

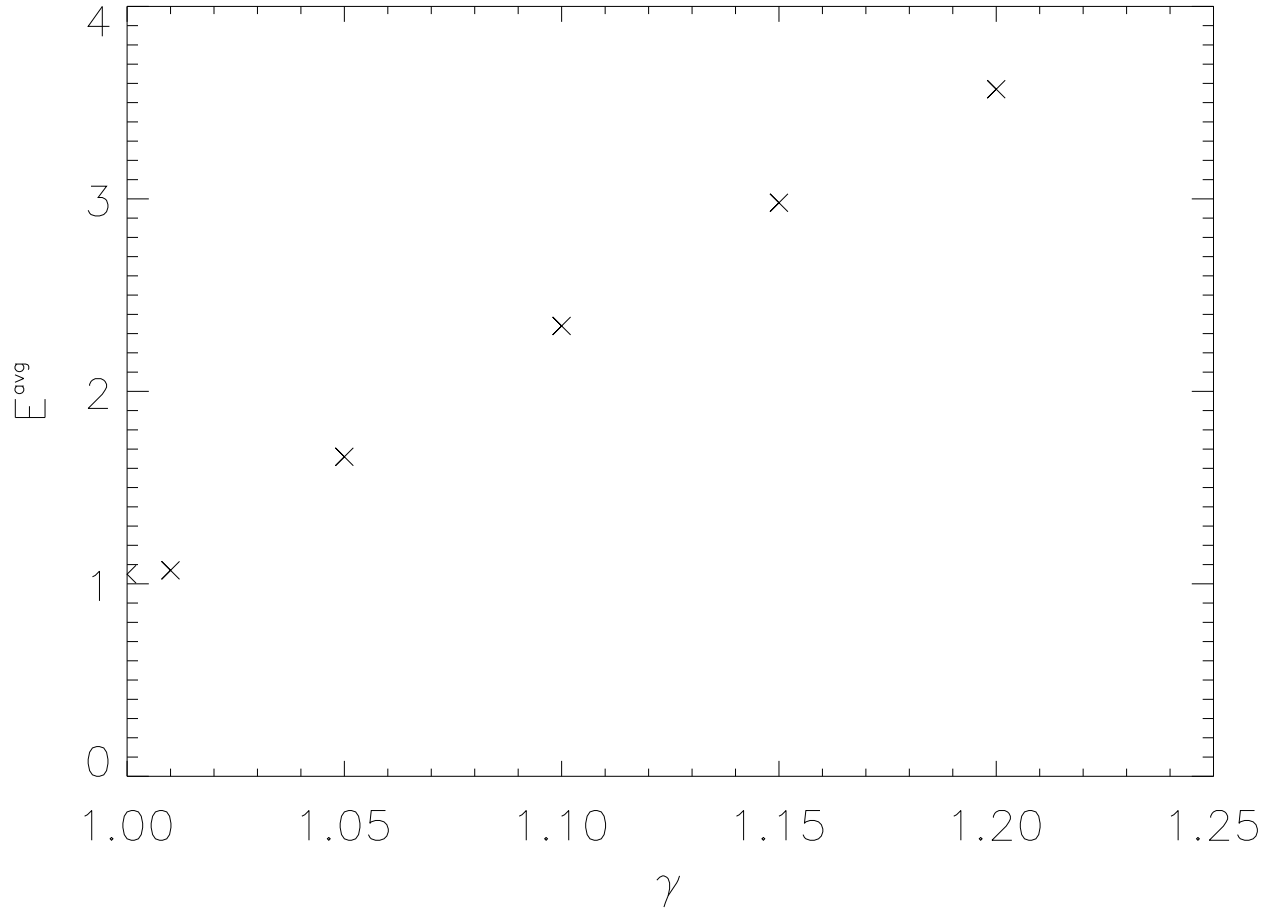


Fig. 7.— The dependence of the  $E_2^{ave}$  on the polytropic index  $\gamma$ . We take  $M = 10^{14}h^{-1}M_{\odot}$  and redshift  $z = 0.1$ .

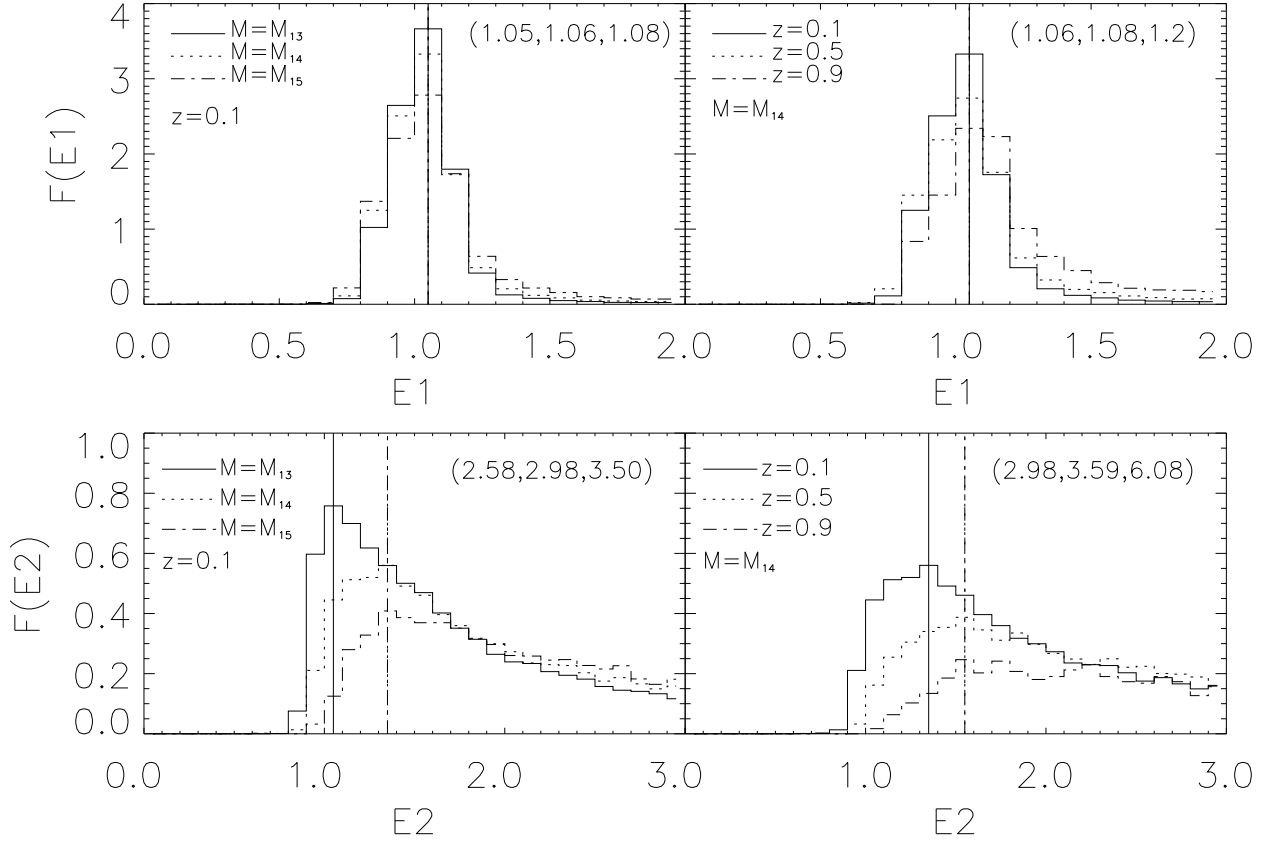


Fig. 8.— Probability distributions  $F(E_1|M, z)$  and  $F(E_2|M, z)$ . The top and bottom panels are for the isothermal and polytropic cases, respectively. The left ones show the dependence of the probabilities on  $M$ , and the right ones demonstrate the change of the probabilities with the change of  $z$ . In each panel, the numbers listed in the parentheses are the average values of  $E_1$  ( $E_2$ ) for the three cases, respectively. The vertical lines show the peak values of  $E_1$  ( $E_2$ ).

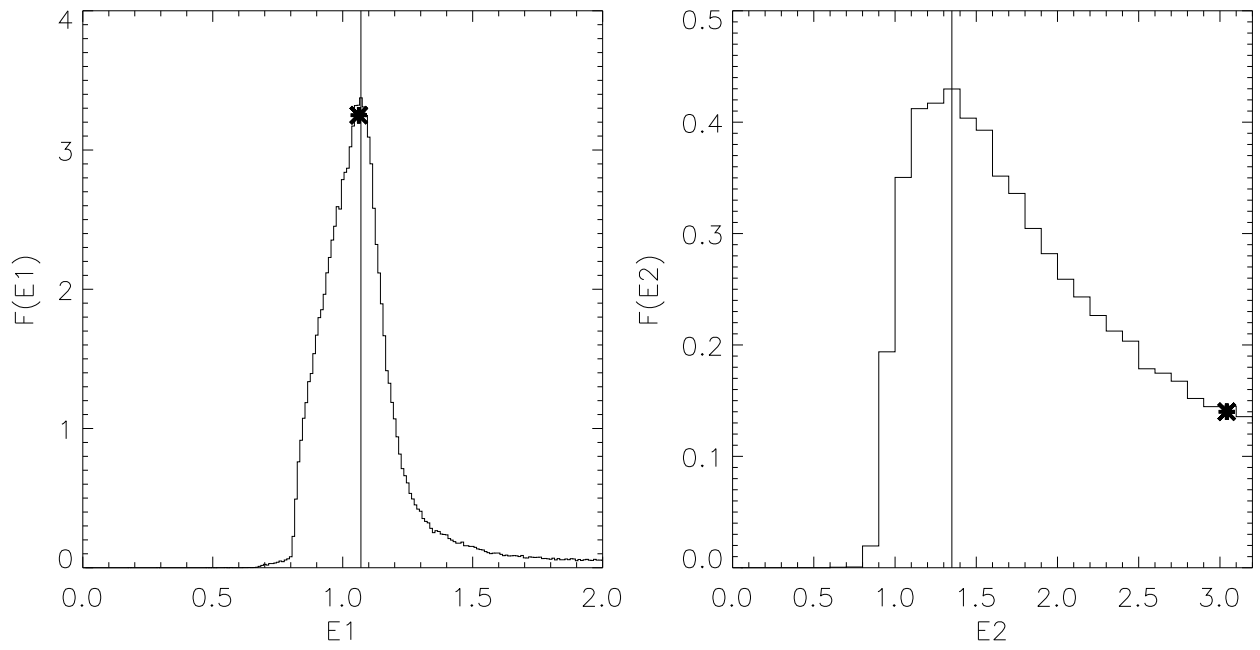


Fig. 9.— Probability functions  $F(E_1)$  and  $F(E_2)$  for mass-limited cluster samples with  $M_{\text{lim}} = 10^{13} h^{-1} M_{\odot}$ . The vertical lines denote the peak values of  $E_1$  and  $E_2$ . The symbols show the average values of  $E_1$  and  $E_2$ .

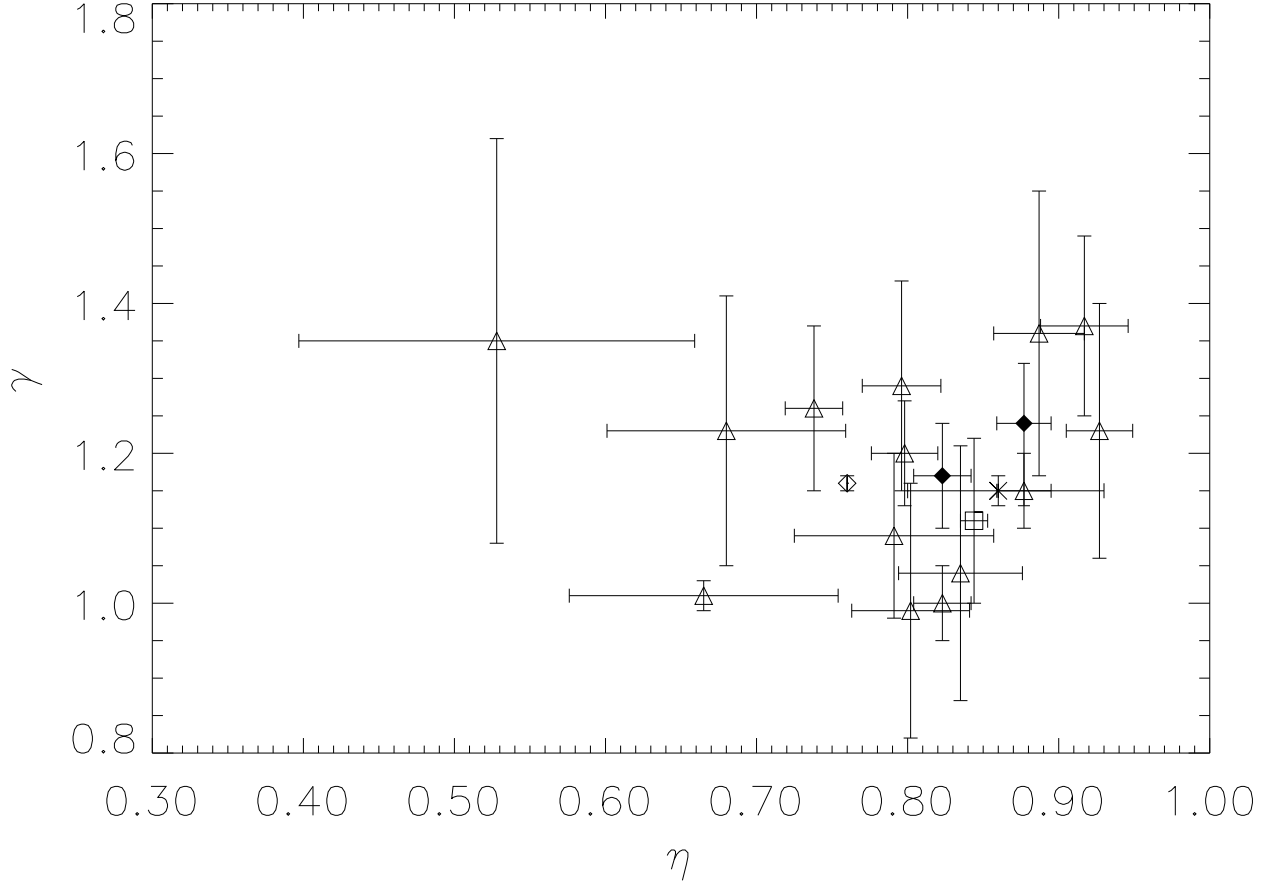


Fig. 10.— Scatter plot of  $\gamma$  versus the axial ratio of the X-ray profile  $\eta$  for 19 clusters. The triangles are from Mohr et al. (1995) ( $\eta$ ) and Finoguenov et al. (2001) ( $\gamma$ ). The filled diamonds are from Mohr et al. (1995) ( $\eta$ ) and Markevitch et al. (1999) ( $\gamma$ ). The square is from De Filippis et al. (2005) ( $\eta$ ) and Finoguenov et al. (2001) ( $\gamma$ ). The cross is from De Filippis et al. (2005) ( $\eta$ ) and Pratt et al. (2005) ( $\gamma$ ). The open diamond is from Belsole et al. (2005) ( $\eta$  and  $\gamma$ ).

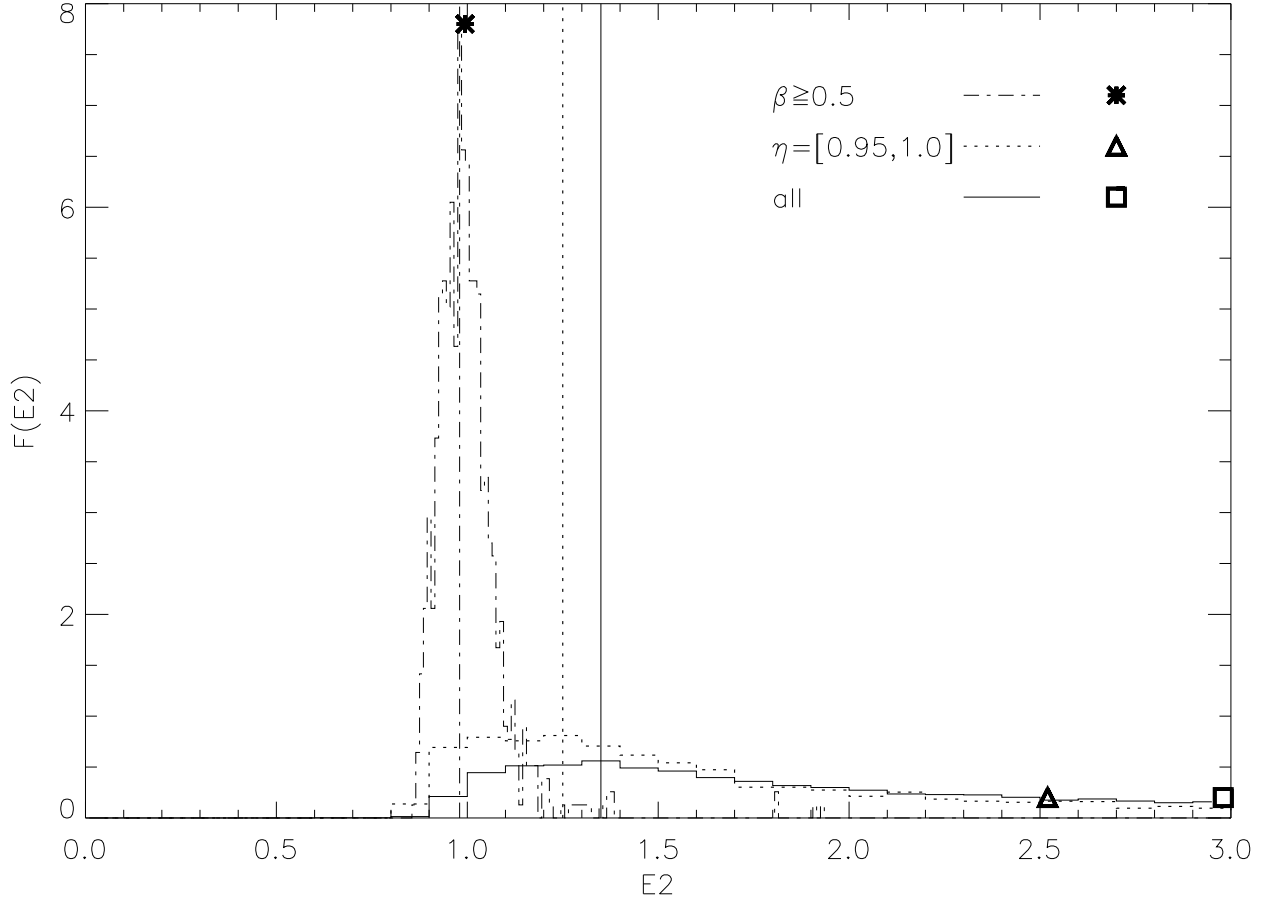


Fig. 11.— The distributions of  $E_2$ . The considered sample of clusters is  $M = 10^{14}h^{-1} M_\odot$  and redshift  $z = 0.1$ . The polytropic index  $\gamma = 1.15$ . The solid, dotted, and dash-dotted lines are for the distributions of the full sample, the subsample with  $\eta \geq 0.95$  and the subsample with  $\beta \geq 0.5$ . The positions of the vertical lines and the symbols indicate the peak values and the average values of  $E_2$  of the corresponding distributions.

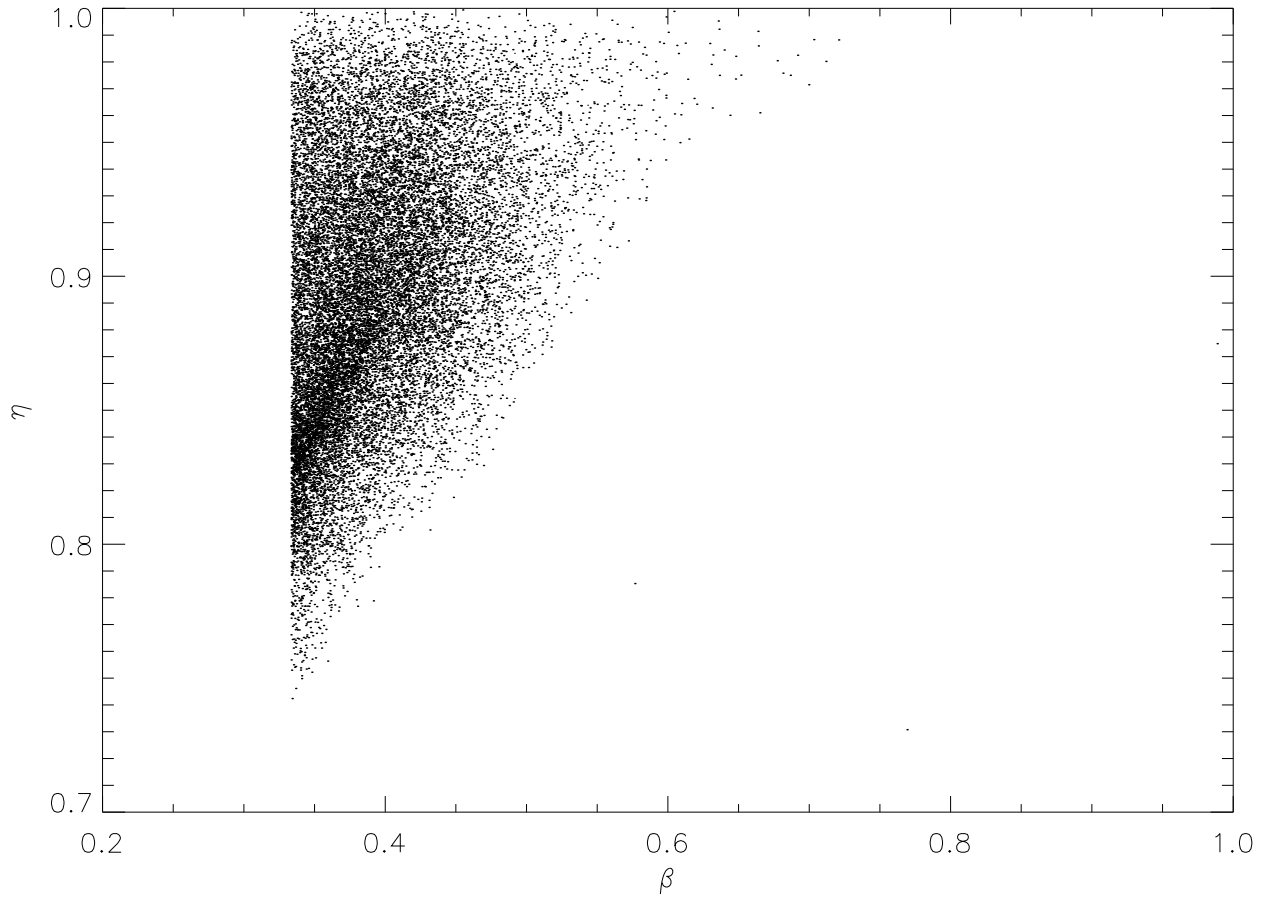


Fig. 12.— The scatter plot of  $\beta$  vs.  $\eta$  for the sample of clusters with  $M = 10^{14}h^{-1} M_{\odot}$  and redshift  $z = 0.1$ . The polytropic index  $\gamma = 1.15$ .

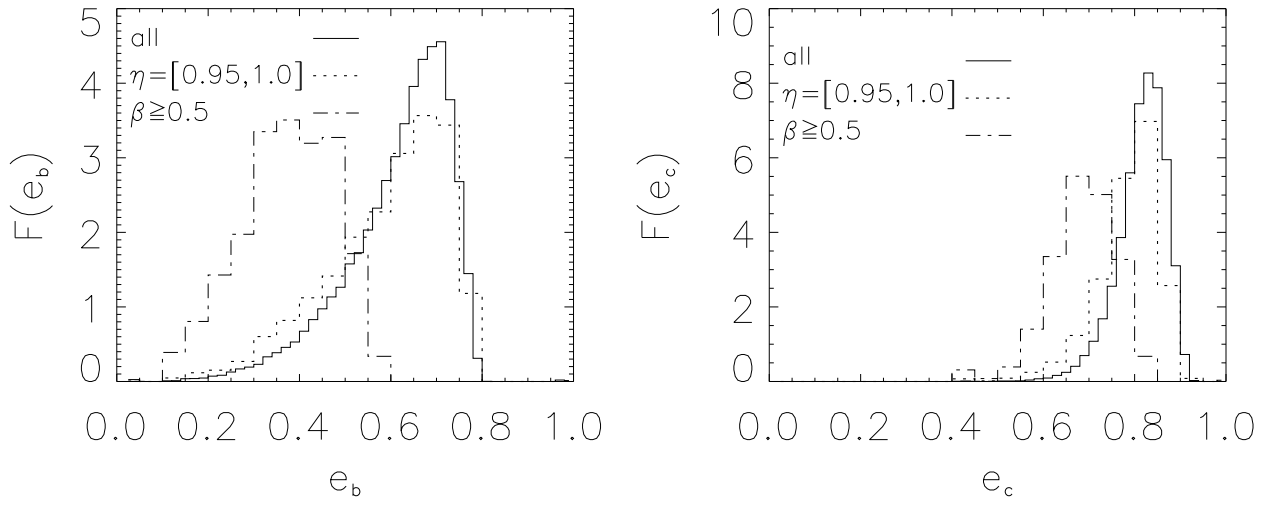


Fig. 13.— The distributions of  $e_b$  (left panel) and  $e_c$  (right panel) for the samples considered in Figure 11.



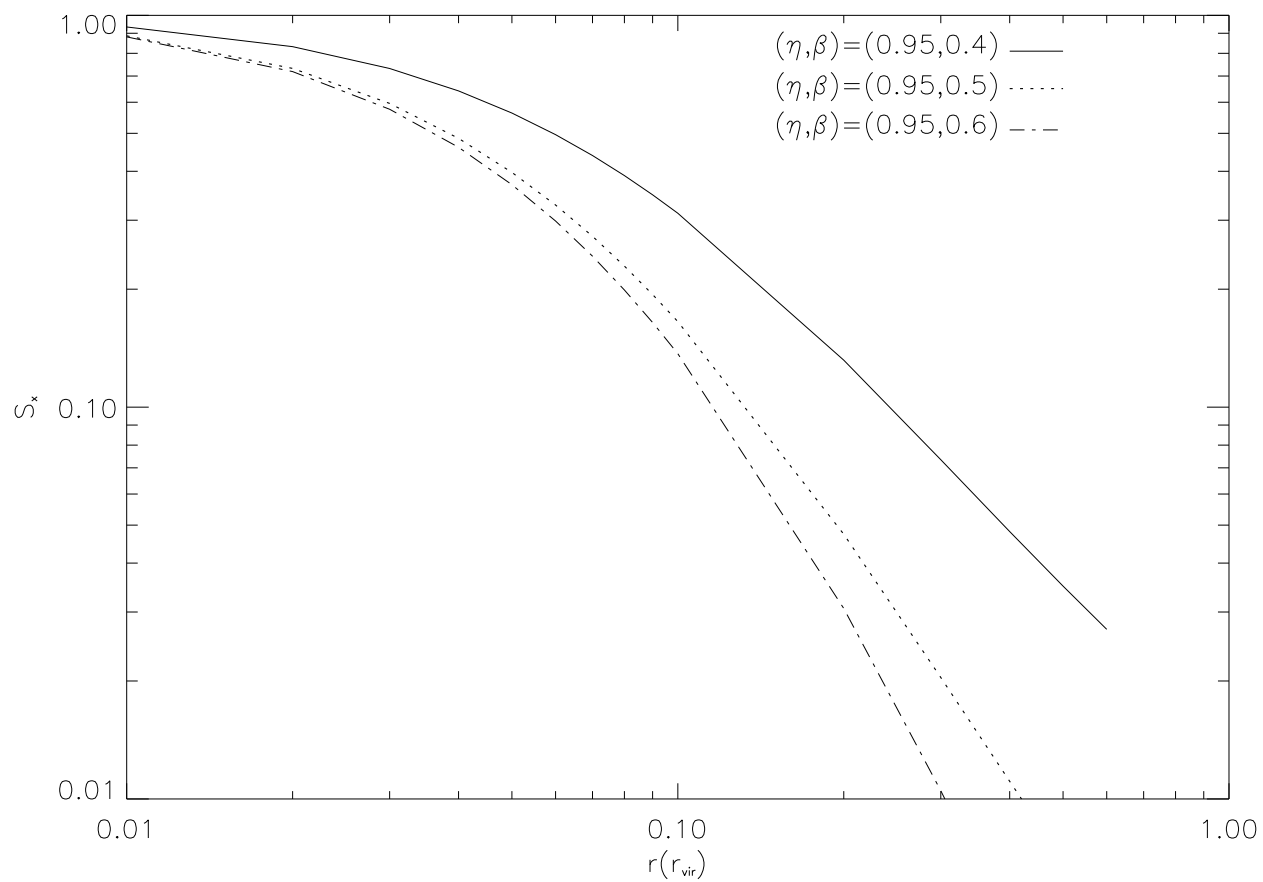


Fig. 14.— The circularized radial profile of X-ray emission for three specific clusters selected from the sample shown in Figure 12. For all the three clusters, we have  $\eta = 0.95$ . The fitted  $\beta$  values are 0.4, 0.5, and 0.6, respectively.